Development of photoelectrochemical devices based in hybrid-perovskites for water splitting reaction

Manuel Felipe Vásquez-Montoya

Faculty of Engineering

Universidad de Antioquia

Director: Professor Franklin Jaramillo Isaza

Advisor: Juan Felipe Montoya Arango

This dissertation is submitted to accomplish the degree of Master in Materials Engineering

Medellín, 2021

To my family

“Learn how to see,

realize that everything connects with everything else”.

Leonardo Da Vinci

Acknowledgments

The achievement of a thesis under a pandemic is not easy and would not be possible without the support and help of many people. I like to use this space to express my gratefulness to them.

I would like to thank my supervisor Prof. Franklin Jaramillo Isaza. For encouraging me to take new challenges, for their continuous support, and for giving me the opportunity to grow at a professional and personal level giving me the thrust to develop my dreams. I would like to special thanks to Dr. Juan Felipe Montoya, for being a continuous advisor, college, and friend, that always trusts in my ideas and envisions. I would also express my gratefulness to Prof. Daniel Ramirez, for their constant support and advisory in this path, making me grow a lot as a professional. I would like to express my utmost thanks to the rest of the CIDEMAT energy line group. To Juan José for being my right hand during all this process. To all the members, Laura, Rafael, Juan Felipe, Esteban, Maria Isabel, Juan Pablo, and Alejandra. For all the interesting coffee discussions, constant advice, and shared experiences. Also specials thanks to Santiago, Franky, and Prof. Jorge Calderon, from the CIDEMAT electrochemistry line for their constant advice, and discussion.

I would like to thank Dr. Eva Unger and Dr. Roel Van de Krol at Helmholtz-Zentrum Berlin, for believing in me and give me the room to live the amazing experience during my research internship. To Janardan and Gopinath on the solar cell division and to Jennifer and Patrik on the solar fuels institute for their constant help and advisory.

I would like to thank my family, my mom, my father, and my brothers, for their unlimited support, love, and company. For always believe in me and trust in my dreams. To my friends, for their continuous support and affection during this journey: Natalia, Carlos, Manuela, Alejandro, Diego, Luis David, and Maria Isabel.

Finally, I acknowledge greatly the Universidad de Antioquia, for financially support my work under the CODI project and “Estudiante Instructor” scholarship. To the DAAD, for financially support my internship and allows me to live that wonderful experience.

List of publications

[1] **Manuel Vásquez-Montoya**. Juan F. Montoya, Daniel Ramirez, Franklin Jaramillo - Understanding the precursor chemistry for one-step deposition of mixed cation perovskite solar cells by methylamine route - *Journal of Energy Chemistry*. (2021) Vol 5, pag 386-391.

[2] **Manuel Vásquez-Montoya**. Juan F. Montoya, Rafael Betancur, Daniel Ramirez, Franklin Jaramillo - Perovskite solar cells: New precursors and challenges for scaling-up - (2021) *Chemical Solution Synthesis for Materials Design and Thin Film Device Applications*. Pag 477-508. Elsevier.

[3] **Manuel Vásquez-Montoya,** Juan F- Montoya, Franklin Jaramillo – Perovskitas híbridas: El futuro de la energía está en la escala nano - *Revista química e industria*. (2019) ISSN 0370-2871. Pag 14-19.

[5] T. Jesper Jacobsson [Other 98 authors including **Manuel Vásquez-Montoya**] The perovskite Database Project: Releasing the power of the crowd with FAIR Data Management. Submitted. Nature Energy

[4] **Manuel Vásquez-Montoya,** Juan J. Patiño, Juan F. Montoya, Daniel Ramirez, Franklin Jaramillo. - Self-supported spray coated NiFe-LDH catalyst for efficient overall water efficiency. Under preparation

Table of contents

Chapter 1:

Introduction

Having a sustainable, robust, and zero-emission energy system is one of the greatest challenges facing humanity; the economic, social, and environmental sustainability of the planet depends on its achievement.[1] Currently, initiatives toward mitigating climate change enjoy of broad support. The international community has embraced the idea in multiple international agreements, including the Sustainability Development Goals (SDGs), Habitat III, and COP21 in Paris[2]–[4]. With COP21, 195 countries adopted the first universal, legally binding global climate deal. It aims to keep "the increase in the global average temperature to well below 2°C above pre-industrial levels and to pursue efforts to limit warming up to 1.5°C by 2050."[5] To reach this ambitious goal, a steep and continuous downward trajectory on global CO_2 emissions from now on is required to reach the net zero goal [4], as shown in Figure 1.1. The energy sector is responsible for 80% of anthropogenic CO_2 emissions, primarily originating from fossil fuels such as oil, carbon and natural gas [6], [7]. Therefore, a radical change in the energy supply and demand must happen in the following years.

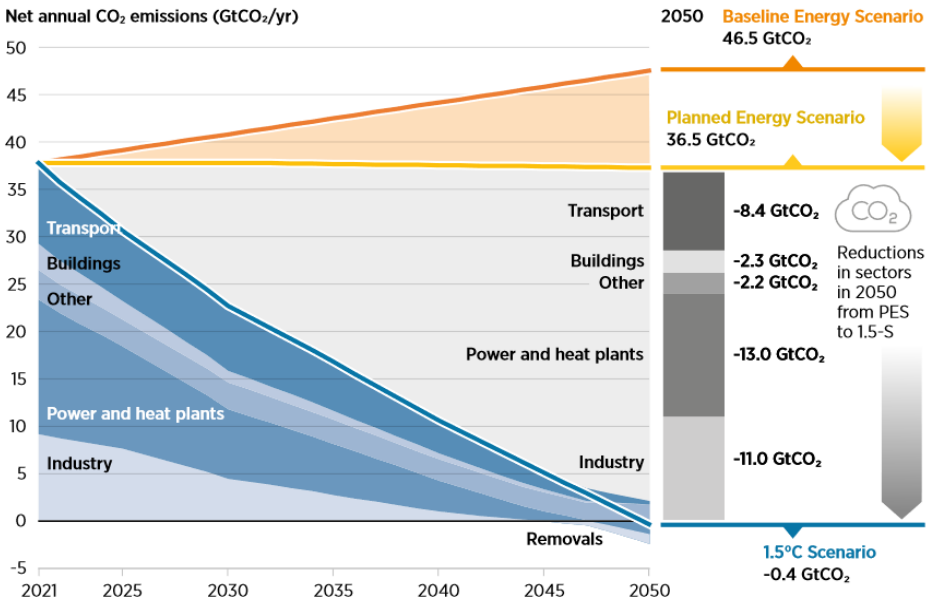

Figure 1.1: Planned strategy to achieve net-zero emissions by 2050, reaching the Paris agreement goal of 1.5°C scenario. Extensive efforts in different energy sectors need to be performed to achieve a rapid reduction on the global emissions. [4]

The changes toward a low-emissions economy are untrivial and must overcome 5 major challenges[2], [8], [9]: i) Increasing renewable energy sources and electricity demand will unbalance the power systems due the intermittency of the resources (i.e. sun and wind). ii) The transportation and energy supply infrastructure need to be modified to ensure a secured energy supply across countries, regions, and cities. iii) Buffering the energy system cannot depend on fossil resources. Hence different reserve carriers must be available to anticipate system imbalances. iv) Several sectors are highly complex to electrify, such as transportation (heavy-duty transport, non-electrified trains, overseas transport, and aviation) energy-intensive industries and residential heating. v) Even if a completely renewable energy system is achieved, it is impossible to replace all the raw materials of the petrochemical industry, fundamental in our modern human society.

Hydrogen is presented as the super star to empower the energetic transition[10], [11]. As an energy carrier, hydrogen tackles the above-mentioned challenges presenting an opportunity to store excess of energy, buffering the grid and supporting renewable integration, additionally it offers a viable solution in sectors where electrification is not possible[8]. These benefits are anticipated by their unique properties[12]: hydrogen is light, storable, reactive, has high energy content per unit mass (141.9 MJ/Kg against the 44.8 MJ/kg from Diesel) and can be used without direct emissions of air pollutants or greenhouse gases.

However, the climate impact of hydrogen depends entirely on how it is made. Three main types of hydrogen are discussed today[7], [13]. First, ‘grey’ hydrogen is made from natural gas, corresponding to the vast majority of currently hydrogen in use, with a demand of more than 70 million tons per year (MtH2/yr)[8]. This process typically emits CO_2, being responsible of around 830 MtCO2/year [4]. Second, ‘blue’, or ‘decarbonized’ hydrogen is made from natural gas with carbon capture and storage (CCS). Despite being a promising strategy to consolidate hydrogen markets and financially support new emerging technologies, CCS is not 100% efficient, their commercial viability is far from represent a reality and the process keeps on depending on the non-renewable gas resource. Finally, ‘green’ or ‘renewable’ hydrogen is made from the electrolysis of water powered by renewable energy. This attractive option has been considerate as the ultimate goal for hydrogen production[3], [14]. Once the hydrogen is produced sustainably, issues will remain concerning storage and transportation of the hydrogen; about cost and efficiency of fuel cells; and about replacing an old, fossil based, infrastructure with a new hydrogen built one[14]. These later problems are, however, subject for other works.

In this work, the sustainable generation of hydrogen was explored using the sun as direct energy resource. Other forms like wind, geothermal, ocean waves or biomass will contribute to the overall hydrogen inventory in the long-term applications but those are out of the scope of this work. Figure 1.2 shows a detailed scheme of the methods to transform solar energy into

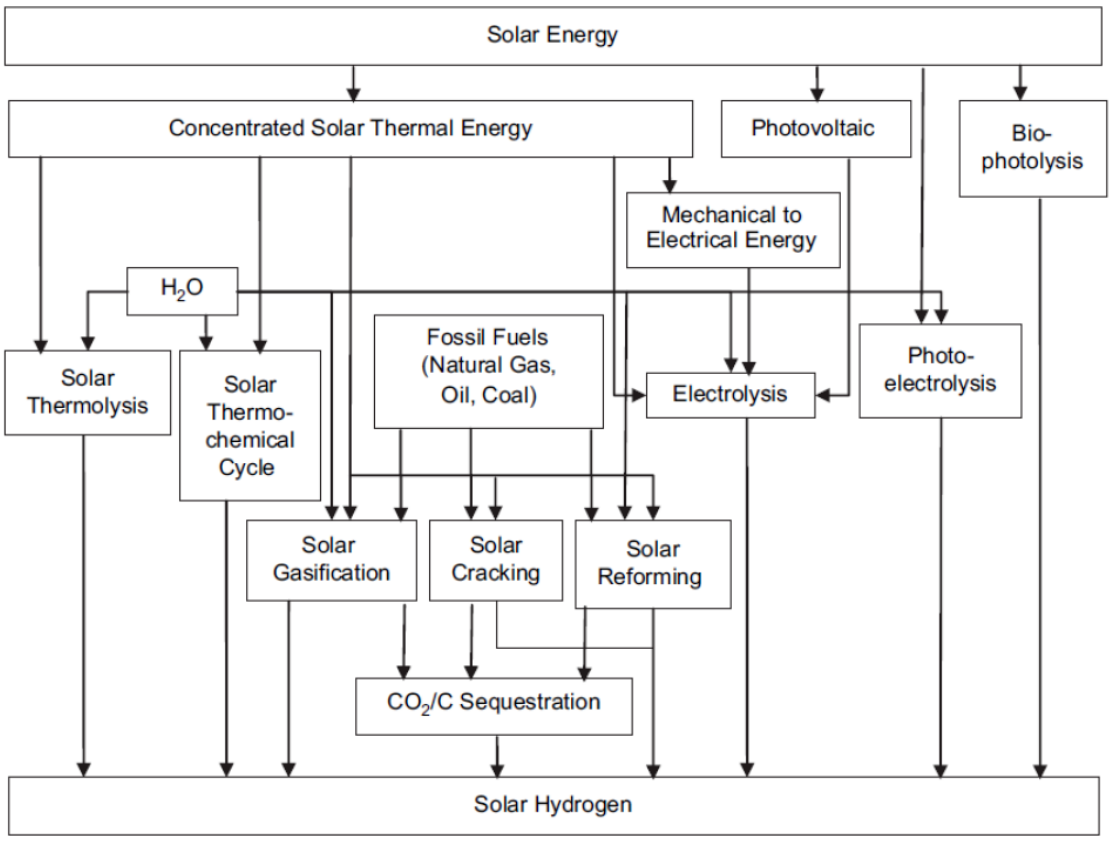

Figure 1.2. Detailed scheme of technologies that uses solar energy as primary resource for the generation of hydrogen[16].

hydrogen[15]. Concentrated solar thermal energy uses high-temperature heat (500°C – 1000°C) from concentrated solar light to drive a chemical reaction that produces hydrogen. The process implements a closed-loop, where the only net reactants are water, producing oxygen and hydrogen[16]. In 2019, the startup Heliogen announced the first commercial prototype for such technology[17]. In photobiological processes, photosynthetic organisms like algae, cyanobacteria, or photosynthetic bacteria, use enzymatic reactions to produce hydrogen at room temperature[18]. However, the efficiencies of these systems are around 1% with low rates of hydrogen production[18]. In this work, our attention will be focused on discussing and developing photoelectrochemical systems where solar energy is transformed into electrons ultimately driving the separation of water in their constituents. This alternative represents the most promising option for the generation of green hydrogen.

1.1. The electrochemistry of water splitting reaction.

The electrochemical separation of water was firstly achieved in 1800 by Nicholson and Carlisle, just a few weeks after Volta fabricated the first batteries[18]. To refer to the separation of water in an electrochemical way, the reaction is divided into two-half reactions, the oxygen

evolution reaction (OER) and the hydrogen evolution reaction (HER), those reactions occur at the anode and cathode, respectively. Under acidic conditions (pH=0 and T=298.15 K), the involved reactions are:

OER (anode)

$$2H_2O(l) \rightarrow O_2(g) + 4H^+ + 4e^- \; ; E°_{ox} = -1.23V$$

HER (cathode)

$$4H^+ + 4e^- \rightarrow 2H_2\,(g) \;\; ; E°_{red} = 0.0\,V$$

Where $E°_{ox\ and}$ $E°_{red}$ represent the standard oxidation and reduction potential of OER and HER at 1 bar. Under alkaline conditions, however, the half reactions are modified, considering now the hydroxide ions. Here the reactions are represented as follows:

OER (anode)

$$4OH^- \rightarrow O_2(g) + 2H_2O\,(l) + 4e^- \; ; E°_{ox} = -0.40V$$

HER (cathode)

$$4H_2O(l) + 4e^- \rightarrow 2H_2(g) + 4OH^- \;\; ; E°_{red} = 0.83\,V$$

To have a pH-dependent scale, the potentials are referred to the reversible hydrogen electrode (RHE), here, the potential is referred as a function of the pH by the Nernst equation: $E_{RHE} = E°_{SHE} - \frac{2.303RT}{F}pH = -0.059pH$ were R is the gas constant, T the temperature, F the faraday constant and SHE refers to the standard hydrogen potential. Therefore, thermodynamically, 1.23 V is the minimum electrical potential required to split water molecules independently of the pH. However, in practical applications, the required potential is much higher (overpotentials) due to the presence of kinetic and engineering issues like activation energy steps, mass transport limitation, internal resistances, etc. These additional parameters are strongly limited by the used pH. Alkaline media induces faster OER kinetics due to the low concentration of protons and high concentration of hydroxide ions, also, the stability of materials on alkaline media is enhanced. Alternatively, acidic media favor a faster HER reaction due to the high concentration of protons and fast mobility of protons reducing mass transfer limitations.

1.2. Electrolyzers and catalyst

On a global scope of the device, the green hydrogen production could be fragmented in 3 main parts: The system level, the stack level, and the cell level. Those are represented in Figure 1.3. The system level, represents all the units involved on the hydrogen production, from the raw material and energy input to the fuel distribution and purification, also denoted as the balance of the system (BOS). On the stack level and cell level, the attention is focused on the electrolyzer, where the electrochemical reactions will take place. Here the anode and cathode electrodes are placed between a membrane that selectively separates the reaction products without affecting the ionic conduction.

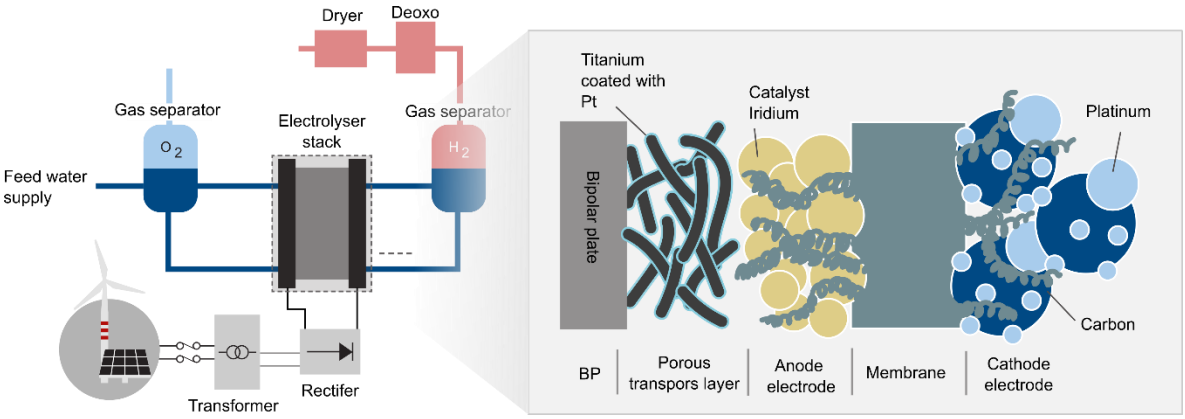

Figure 1.3: List of overpotentials required for different electrocatalysts in acid and basic media, for the OER and HER reactions.[33]

To improve the overpotential of the water splitting reactions, a catalyst is added to modify the energetic requirements associated with the activation energy barriers. Compared to the HER, the OER is far more complicated from a kinetic perspective, due the sluggish kinetics and high-activation energies of four-electron transfer processes[19]. In alkaline media, which is the pH used in this thesis, the mechanism adopted for the reaction was introduced by Rossmeisl and Noskov[20]–[22]. This mechanism follows the next 4 reactions.

$$M^* + OH^- \rightleftarrows M - OH^* + e^- \quad (1)$$

$$M - OH^* + OH^- \rightleftarrows M - O^* + H_2O + e^- \quad (2)$$

$$M - O^* + OH^- \rightleftarrows M - OOH^* + e^- \quad (3)$$

$$M - OOH^* + OH^- \rightleftarrows M^* + O_2 + H_2O + e^- \quad (4)$$

The superscript "*" indicates the active metal site (M*) or the adsorbed intermediate. Each step involves one electron transfer (ET). At each reaction, the oxidation state of the metal ion at the active site may change, with the metal undergoing either oxidation or reduction or the metal oxidation state remaining unchanged. Additionally, there are pure chemical steps between ET that also occur, especially when a rapid discharge step is followed by a slow bond-restructuring process[23]. Regarding the OER mechanism, a strong debate prevails and different experimental and theoretical efforts have been made to reduce the overpotential caused by these reactions[24], [25]. For the HER, the reactions follow a 2-electron transfer process. Here, two mechanisms have been widely adopted: the Volmer-Tafel and the Volmer-Heyrovsky mechanisms[23]. On alkaline media these reactions are[26], [27]:

$$H_2O + M + e^- \rightarrow M - H_{ads} + OH^- \ (Volmer)$$

$$2\ (M - H_{ads}) \rightarrow 2M + H_2\ (Tafel)$$

$$H_2O + M - H_{ads} + e^- \rightarrow H_2 + M + OH^-\ (Heyrovsky)$$

Here, M refers to the metal oxide surface and the M-H_{ads} depicts hydrogen intermediates adsorbed on the electrode surface. To more insights about the mechanism and details in the water splitting mechanism, please refer to the work of Bockris et al. [28], Zhang et al. [20] or Song et al. [29].

Unfortunately, the catalyst that has demonstrated the lowest overpotentials and highest exchange currents is based on rare and expensive noble metals such as platinum and RuO_2 for HER and IrO_2 for OER[30]. Extensive efforts have been devoted on explore earth-abundant, efficient, and inexpensive catalysts. Many cheap and earth-abundant transition-metal-based materials have been explored as potential electrocatalysts for the OER and HER in the past few decades[31], [32]. Some examples in basic and acid media are shown in Figure 1.4. Among these catalysts, transition metal oxides[33] and (oxy) hydroxides[34] receive widespread attention due to their significant catalytic performance toward the OER. They possess high electrical conductivity and structural stability when operating in alkaline solutions making them excellent candidates for water splitting[35]. Chapter 3 will explore the development on this type of catalysts.

1.3. Semiconductors and solar cells

So far, previous sections show how to separate the water molecules using an electrical input. Referring to the solar energy, the electrical input is generated through the absorption of photons by a semiconductor to transform it to electrical energy. Here 4 fundamental steps must happen

to ensure the obtention of photoinduced work[36]: light absorption, carrier separation, carrier transport and collection.

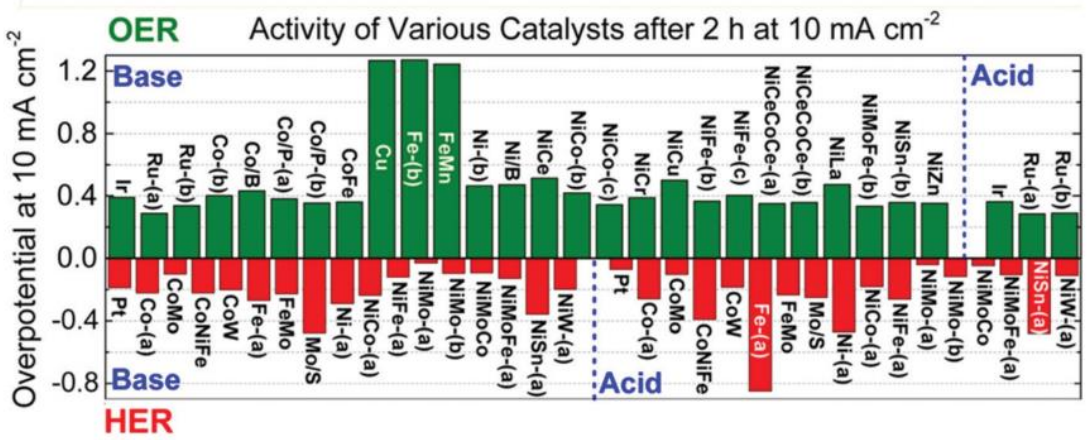

Figure 1.4: List of overpotentials required for different electrocatalysts in acid and basic media, for the OER and HER reactions.[33]

When a photon with an energy higher than the bandgap of the material is absorbed, electrons are promoted from the valence band to the conduction band. Here, the carriers are created, named as electrons with negative charge and holes with positive charge[37]. The number of generated carriers will be a direct function of the band gap, the absorption coefficient, and the irradiated flux spectra[38]. After the excitation process, carriers must be separated before they recombine. This separation could occur by different mechanisms[36], [37], [39] like drift (movement of electrons due an electric field), diffusion (movement due concentration gradients) or recently polarons (movement due the distortion of a polarized lattice)[40]. Fine-tuning strategies of the energetic structure of the device like building up p-n junctions[41], the addition of selective transport layers[42], or adding external bias[43], allows to maximize the charge separation limiting recombination. Once separated, the charges need to be transported through the semiconductor interface to allow the final charge collection. This transport will also be influenced by the electric field and concentration of carriers built in the structure[44]. Moreover, the transport distances could vary on the system (from nanometers to micrometers) and will ultimate depend on the system resistance and recombination on the materials[45]. This recombination will be strongly affected by defects, grain boundaries, or interface defects[46]. Ultimately, the charges are collected by a metal or redox system to complete the electrical circuit.

As mentioned earlier in this chapter, the minimum amount of energy for driving the water-splitting reaction is 1.23 eV. This means that only photons with greater energy ($\lambda < 1010$nm) are capable to generate photo-exited charge carriers and carry reactions at the interface electrolyte-semiconductor[38]. Adding kinetic overpotentials and losses in the device, a single

junction device must have a bang-gap between 1.6-2.4 eV to drive this reaction. Plus, the position of the band edges is of importance. Semiconductor must straddle the redox levels for water, and the proper alignment of the band determines the band bending, further separation and transport of the charges. This introduces additional constraints and further narrows down the set of semiconductors with suitable optical properties that could be of interest. Some semiconductors studied in this regard are TiO_2[47] , $BiVO_4$[48], Fe_2O_3[49], and CuO[49].

A strategy to circumvent the problem with the solar spectrum mismatch encountered for one band gap, single-cell devices, is to fabricate tandem devices, where two or more semiconductors with different band gaps are stacked on top of each other[50]. Here, the light absorption is more carefully managed, allowing that losses associated with thermalization are reduced[51]. A tandem cell can absorb a greater part of the solar spectrum compared to a single band gap device; in spite of that as a high photo-potential can be generated. Nonetheless, the semiconductor band-alignment is challenging, and the system complexity increased dramatically, increasing costs, and narrowing the fields of application[52]. Another approach to solve the solar spectrum mismatch problem is to interconnect several single band gap cells in different configurations[53]. In this way, the required voltage and current could be supplied by arranging the device in series or parallel configurations, depending on the employed semiconductor absorber[54].

1.4. Photoelectrochemical systems

Considering the integration of the semiconductor and catalyst to drive on the water splitting reaction, there are three options as shown in Figure 1.5: Photovoltaic+electrolyzer (PV+E), photoelectrochemical cells (PEC) and particulate photocatalyst.

In the PV+E, the semiconductor is located outside the electrolyte and therefore, the performance of the cell is completely independent of the character of any solid/electrolyte interface[55]. The light absorber is completely out of water, and hence, stability against corrosion in the aqueous medium is of little concern[56]. Also, sizes of PV and electrolyzer components (EC) can be freely modulated because they have different balance of system (BOS). The BOS denotes auxiliary components needed for operating the device such as piping, controller, fuel or charge transfer roads[14]. For the PEC systems, the semiconductor is immersed in the electrolyte, when an electrolyte-semiconductor junction is formed, the photovoltage and photocurrent produced in the presence of light arise from the differences in the electrochemical potentials of the solid and the electrolyte, as well as from asymmetries in the charge-transfer kinetics for electrons and holes across the junction. Electrocatalysts could be used in the device to enhance the charge transfer kinetics, but the operation of the device will still rely in the electrolyte-semiconductor interface[55]. Finally, the particulate photocatalyst powders are dispersed in the medium, and thus the charge transfer pathway is

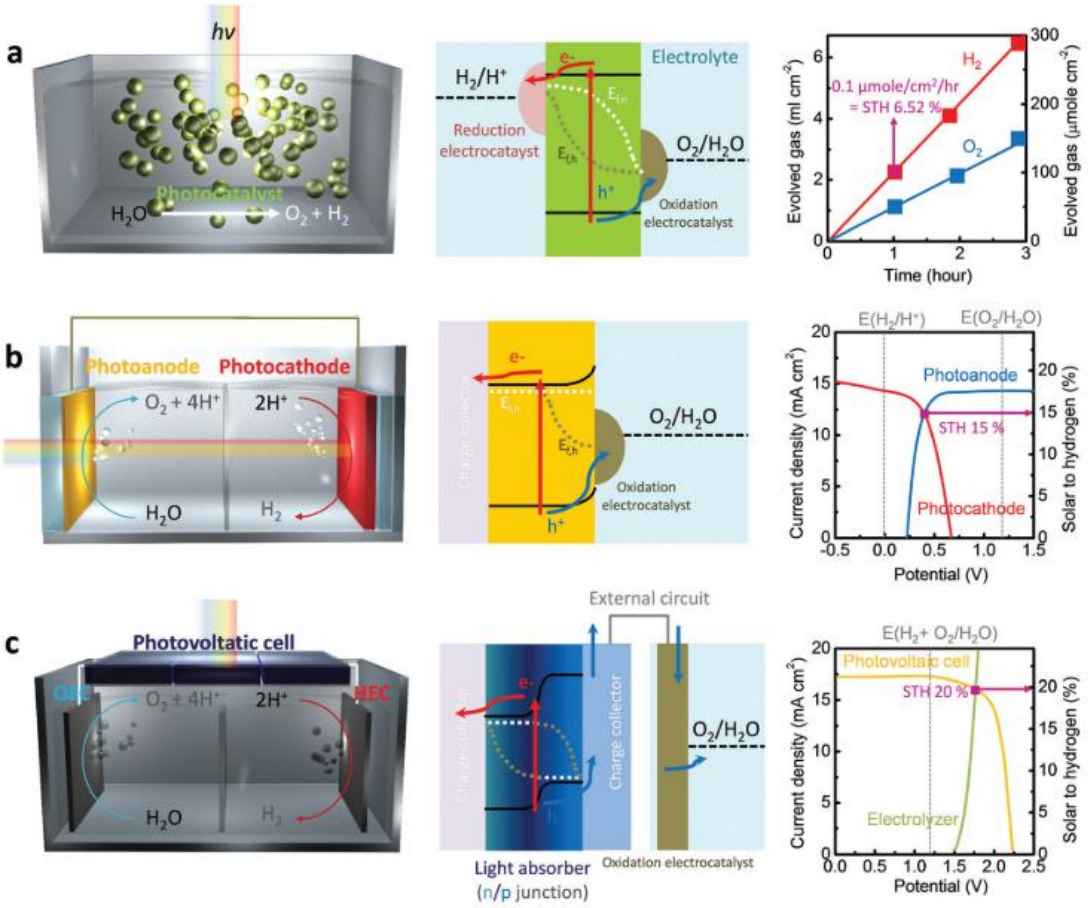

Figure 1.5. Graphical representation of the main photoelectrochemical systems, with the energetic considerations and figure of merit of each system. a) photocatalyst configuration, b) PEC system and c) PV+E configuration [12]

significantly shorter (several micrometers or nanometers) than usual charge collectors in the other systems (sometimes tens of meters)[57], [58]. Each unit individually absorbs light, generates excited carriers and performs the desired chemical reactions at the particulate/molecular electrolyte interface, significantly reducing the system complexity but lowering drastically the overall efficiency[59]. Important advances have been made in the photocatalysis field in this direction but those are out of the scope of this thesis.

Different perspectives, including economical, physical, and engineering ones – must be evaluated in searching for the optimal configuration. The common argument in favor of the PEC cell research is based on an economical benefit from the device structure integration. Nonetheless, with the drastically reduction on photovoltaic prices and the economy of scale of electrolyzers, this argument is hard to maintain. Recent techno-economic studies have pointed a levelized production cost of hydrogen (LCOH) for PV+E at 6.22 $/kg H2 versus 8.43 $/kg H_2 for PEC[60]. One should also consider that BOS costs for collecting hydrogen with pipes

and membranes over large solar collection areas will likely be much higher than those for a PV-electrolysis installation (even though there may be some savings on the inverters)[61]. Nonetheless, the technological readiness level of the PEC system is still very low, and a lot of uncertainties make difficult to predict the final cost and decide for the best technology[12]. Therefore, technical arguments must be also considered on the discussion. PEC cells operate at very low currents (10-20 mA/cm^2), 100 times lower than conventional electrolyzers (1-2 A/cm^2). This feature increases the internal electrolysis efficiency, requiring less overpotential for the reaction. Also, the stability of the catalyst is further enhanced, losses for bubbles are diminished and the possibility of membrane-less devices are more facile to consider[62]. Nonetheless, operating at low currents will demand a very large area to supply the same PV+E hydrogen production[23], but their impact in the final cost need to be evaluated. Another benefit of the PEC relies on the thermal management. Solar cells have a drastically effect on temperature, operating at 60°C-80°C the devices could reduce their efficiency in up to 10%[63]. In PEC, the immersion of the absorber in the electrolyte allows a more effective heat transfer to the solution. Not only reducing the losses on the photo absorber, but also improving the reaction kinetics by 2 per 10°C increase (Arrhenius law)[61]. Studies have shown that the improvement in the kinetics is larger than the decrease in the photovoltaic properties of the PEC absorber[64].

In a critical analysis, presented later in chapter 4, previous benefits of PEC could be also applied to PV+E systems following a different engineering approach. Therefore, the actual distinction between the systems must rely on a more fundamental level. The PEC and PV+E differ in a small but important detail: the formation of the electrolyte/solid junction[55]. Therefore, a PEC configuration will be preferable if the electrolyte/solid junction present any benefit in the efficiency of the final device. This benefit could be in two forms: (i) improving the operation potential of the semiconductor or (ii) modifying the kinetics of the reaction. In theory, when a semiconductor is in contact with the electrolyte, it forms a nearly ideal junction[65]. This junction will reduce interfacial losses that otherwise could affect a PV device and therefore, allows a more efficient and simpler device. In the second option, photocatalytic studies have been demonstrated that a light induced photocatalyst could be more efficient than only an electrocatalyst exploding quantum mechanical effects like hot carriers[66]–[68]. Thus, considering excited states, the energetic barrier could be reduced and therefore, less overpotentials are necessary for the reaction[19]. These concepts are still far from the real application on PEC devices, but the research of new materials must account this fundamental concepts. Without this clear goal, the collective advance of the PEC technology will be stacked, and, in the end, the challenge of global warming depends in having as many options as possible to sustain our global energy system. In this thesis, the analysis of both conditions PV+E and PEC are presented for a very special family of semiconductors, the lead halide perovskite semiconductors.

1.5. Lead halide perovskite semiconductors

Until now, no single-junction material has been capable to supply the water splitting reaction potential without any additional bias. Thus, the key research needed for solar fuels generators based on PEC cells involve the discovery and development of semiconducting materials that possess both the proper band gaps for effective sunlight absorption and well-positioned band energetics to perform the water splitting reactions. Additionally, key features such as earth-abundant materials-based and large-scale production economy are crucial to make PEC devices economically competitive against the PV+E systems[69], [70].

Lead halide perovskites have revolutionized the solar cell industry due to their amazing semiconductor properties. This group of materials follows the perovskite structure ABX3, where A is a cation (including organic like $CH_3NH_3^+$, $CH(NH_2)^{2+}$ or inorganic Cs^+, Rb^+), B is a metallic cation (Pb^{+2} or Sn^{+2}) and X a halide anion (I^-, Br^-, or Cl^-). This material possesses excellent optoelectronic properties such as high incident light absorption capacity (absorption coefficients in the order of 10^4 - 10^5 cm^{-1}), and high charge transport and mobility[71]–[74]. Moreover, this family of materials is constituted by earth-abundant elements and their devices can be manufactured by continuous printing methods, such as ink-jet printing, slot-die coating, among others, compatible with roll-to-roll processing[75]. Additional concerns with lead content on the perovskite absorbers have to be addressed but interesting advances towards tin-based perovskites or double perovskites had gained important advances in the last years[76].

These semiconductors have been implemented on photoelectrochemical cell research. In 2012, Luo et al[77] reported a PV+electrolyzer using 2 series of MAPbI3 connected solar cells with NiFe LDH catalyst to obtain a solar to hydrogen conversion of 12.3%. Recently, astonishing efficiency of 18.7% have been obtained using a silicon/perovskite tandem device connected to NiFe and TiC/Pt catalysts[78]. A roadmap to achieve over 20% efficient devices have been proposed, hopefully beating the state-of-the-art devices based in III-V semiconductors[79]. Perovskite devices also have been studied in integrated devices. To protect perovskite from direct contact with the electrolyte, 3 main options have been implemented: i) atomic layer deposition coatings (ALD), ii) metallic electrode encapsulation and iii) carbon electrode encapsulation.

Kim et al[80], fabricated a photocathode using a layer of titanium dioxide deposited by atomic layer deposition (ALD) as protection layer. On this approach, authors used thin platinum as co-catalyst in the photoelectrode measurements. With this configuration current density of 10.5 mA cm^{-2} at 0V vs RHE and a stability of 2h was achieved. This work is the only report where a perovskite device is made to preserve the electrolyte/semiconductor junction. In a second

approach, metals are known to provide absolute protection against moisture. Linked to this idea, Crespo-Quesada[81] et al used a Fields metal (InBiSn) together with a platinum catalyst deposited on the surface to elaborate a photocathode. With this strategy, hydrogen generation is achieved with a current density of -9.8mA/cm^{-2} and a stability of approximately 1h. It has been proven that hybrid perovskite is susceptible to metal ion migration, resulting in corrosion by products such as metal halides[82]. For this reason, the long-term stability is strongly compromised in this type of configurations. Another approach to use metals as encapsulants have been explored like Ni[83] or Ti[84].

Finally, one of the strategies that has gained momentum is the use of hydrophobic carbon to protect the hybrid perovskite. Poli et al[85], fabricated a photoanode using a carbon bilayer joining mesoporous carbon and graphite to protect $CsPbBr_3$-based perovskite, obtaining a stability of more than 30h and current densities higher than 2.5mA/cm^2 at 1.24V against the normal hydrogen electrode. Another example is reported by Tao et al[86], where they managed to obtain a stability of more than 12 h in different electrolytes and a current of 12.4 mA/cm^2 at 1.23V. The great advantages of this approach are its stability in contact with perovskite, its high surface area for catalyst loading and the possibility of implementing them by industrial printing methods such as screen-printing or doctor-blade.

1.6. Aim of this thesis.

Recognizing the special potential of halide perovskite semiconductor as a material suitable for large scale production and outperformance efficiency, and the requirement for sustainable production of green hydrogen, this project aimed to integrate this semiconductor to photoelectrochemical devices for water splitting reaction. This thesis is written as a stand-alone section, focusing on special challenges for the main components: Perovskite absorber and catalyst fabrication. On the end, the integration of both advances is presented to outlook the requirements for integrate the components on a real device.

On the second chapter, the fabrication of the perovskite absorber is covered, here, different compositions are explored looking for large-scale production and high-performance devices. On this sight, the bication perovskite using methylamine was selected as a solvent for the perovskite production. Here, an interesting correlation between the solvent amount and the final crystallization phases of the perovskites was found.

On the third chapter, the methods to fabricate and implement state-of-the-art catalyst compatible with large scale deposition methods was presented. Here, successfully synthesis of NiFe-LDH catalyst was obtained, with outstanding catalytic performance for oxygen and hydrogen evolution reaction using scalable coating methods like spray-coating or dip-coating.

On the fourth chapter, the integration of the perovskite and catalyst on a photoelectrochemical device was introduced. First, an PV+electrolyzer system was obtained with a remarkable STH efficiency of 10.4%. Herein, an analysis about the non-viability of conductor-based protection

strategies was presented and externally connected devices exactly reproduce the reported devices performance. In the end of this chapter, semiconductor-based protection strategies using TiO_2 by ALD or IZO by sputtering was introduced. These steps suggest a route to further integrate the perovskite absorbers as suitable semiconductors for photoelectrochemical water splitting devices.

Chapter 2:

Looking for scalable perovskite absorbers

Expanding compositional range on methylamine perovskite precursors

2.1. Introduction

On the roadmap of an efficient photoelectrochemical system, the absorber represents the heart of the operation. According to the processes summarized in the introduction, the overall progression of solar hydrogen production was divided into four fundamental steps: Charge carrier generation, separation, transport, and interfacial reaction. Comparing these steps with a solar cell; the first three are identical. Therefore, fabricating an efficient solar cell device is a crucial step for the goal of photoelectrochemical device construction. Metal halide perovskites (MHP) have attracted attention recently due to their low cost and easy solution processability coupled with interesting photophysical properties such as long carrier diffusion lengths, high mobilities, direct and tunable band gap, high absorption coefficient and unusual tolerance to defects.[71], [87], [88] As a result, perovskite solar cells (PSC) have reached record photovoltaic conversion efficiency (PCE) of 25.5%[89]. Nonetheless, the perovskite literature is overwhelming with more than 5500 unique devices combinations and 400 families of perovskites successfully implemented in solar cell devices[90]. Therefore, an important question emerges. Which is the best choice for the perovskite composition aiming to scalable and high-efficient devices?

A hint to answer that question arises from the chemical nature of the process. The careful control of precursor chemistry, and the morphological and crystalline properties of perovskite films have made possible highly efficient PSCs. Crystallization techniques including antisolvent[91], gas quenching [92], [93] , vacuum drying [94], and infrared annealing [95] have been optimized for depositing smooth, highly crystalline and defect-free perovskite films. Unfortunately, these set of techniques work effectively for depositing perovskite films by spin-coating but are hardly compatible with scalable techniques such as blade or slot die coating [96]. Due to the strong coordination ability of PbI_2 and the high boiling point of the typical perovskite precursor solvents (i.e. DMF, DMSO),[97] the traditional crystallization techniques rely on external forces for drying the film. Moreover, they have a narrow operation window, which hampers their reproducible transference to roll-to-roll (R2R) systems.

Recently, researchers have reported the deposition of perovskite films by R2R or blade coating using a precursor composed of a mixed solvent of methylamine (MA) and acetonitrile

(ACN). [96], [98], [99] Using this precursor, the above-mentioned drawbacks have been overcome by allowing one-step deposition of perovskite films with optimal morphology over large area substrates. The advantage of this precursor relies on the strong coordination interaction of MA with PbI_6^- clusters combined with hydrogen bonding with the $CH_3NH_3^+$ (MA^+) cations at A-sites of the $MAPbI_3$ perovskite.[100]–[104]As a result, stable solutions of $MAPbI_3$ in mixed solvents including MA/ACN [105] and MA/Tetrahydrofuran (THF) [106] has been reported. Under these solvents, the desirable properties for perovskite precursors such as surface tension, and boiling point were achieved.

Several methods have been implemented to incorporate MA and fabricate high-quality $MAPbI_3$ films, as depicted in Figure 2.1. Nakita et al. [107], proposed the bubbling method, where the perovskite precursors in ACN solution are bubbled with methylamine using N_2 as the carrier gas until a clear solution is observed. Another option is to leave perovskite powder or crystals in a sealed vessel with methylamine solution, here, the methylamine diffuses and reach the perovskite material forming a viscous solution. Here, the formed liquid can be diluted in a proper solvent (dilution method)[99], [108] or applied in the substrate using mechanical pressure (peeling method)[109]. The last option, referred here as degassing method [110], is a post-treatment of raw perovskite films that are exposed to MA gas. This leads to a fast conversion into a bleached film, then after removing the MA gas, the film returns to its initial state with improved morphology and crystallinity. Note that the MA precursors have been deposited by spin-coating, blade-coating, dip-coating, or slot-die technique.

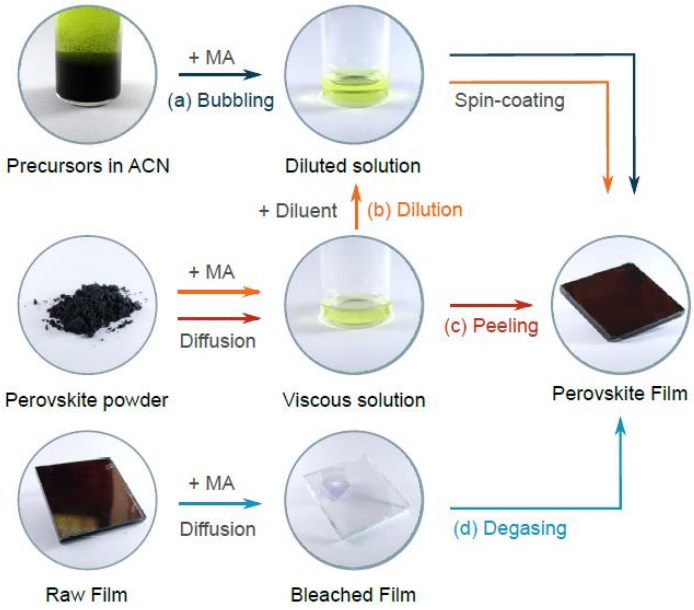

Figure 2.1. State of the art methods for incorporation of methylamine into $MAPbI_3$ perovskite

Despite the successful development of the MA based precursors, their application has been limited to deposit $MAPbI_3$ perovskites. One of the most successful methods to enhance the stability of perovskite materials is A-site cation engineering, leading to the most efficient and stable perovskites reported to date.[111] The best PSC devices are based on perovskites with A-site cation combinations of formamidinium (FA^+), Cesium (Cs), methylammonium (MA^+) or rubidium (Rb). [112]–[114] Most of these multication perovskites have been processed by solvent engineering, but there are few reports on multication perovskites processed in the MA based solvent. Zhao, et al. report that MA exposure into $FAPbI_3$ films rapidly forms a bleached film, but their back conversion upon degasification is sluggish [115]. Benjia, et al. [96] fabricated efficient blade-coated $MA_{0.875}FA_{0.125}PbI_3$ perovskites using the bubbling method with PCE of 18%, but as proved earlier by Zhang et al.[116], small amounts of formamidinum cation in the presence of MA form passivating structures of δ-$FAPbI_3$ rather than active perovskite phases. Therefore, there is still a significant lack of understanding of mixed A-cation perovskite in methylamine solvent.

In this chapter, the requirements to stabilize multication perovskite films with high FA^+ content based on MA precursors was explored, looking into high-efficient and scalable devices. Initially, the consequences of the methylamine incorporation method in the phase stabilization was explored. Viscous-stage related methods were the only way to stabilize the α-phase perovskite due to the increased MA incorporation. By tuning the MA ratio in the precursors, a dependence with the amount of MA was found. Here**,** at a small amount of MA, crystallization favors the formation of 1D FA_3PbI_5 phase and 2H/4H polymorphs. In contrast, at high MA amounts, crystallization leads to films with solely α-phase perovskite. Moreover, this behavior was attributed to the formation of FA^+ - MA complexes that fully determine the final crystallization phase. This understanding open the window for developing controllable precursors applicable to one-step deposition of mixed cation perovskites for large-scale processing. Finally, an overlook to other compositions non-explored in the MA literature was discussed and results of efficient devices following typical precursor compositions was presented.

2.2. Experimental

2.2.1. Perovskite powder preparation

The perovskite powders were prepared following a modified procedure by Zhang[117]. Here, 688 mg of FAI and 167 mg of MAI were dissolved in 10 mL of ACN. An excess of 5% of methylammonium iodide was added to the precursors to ensure full conversion in the reaction. Afterward, 2305 mg of PbI_2 was rapidly added to the solution, and constantly shaken for 10 min. Different color transitions are observed upon final transition to the black perovskite phase. Finally, the product was dried at 100°C for 20 min and stored in the glovebox for further use. A yield of around 90% was achieved with this method.

2.2.2. Perovskite solution fabrication

400 mg of powder was placed in a vial, with 3mL of methylamine solution in a ceramic cresol and held in a 1470 mL (10 cm height) hermetic jar during different times to ensure a different amount of methylamine incorporation. This process must be held in non-reactive materials like ceramics due the high reactivity of MA gas. The ratio of methylamine incorporated in the solution was determined by the mass difference, before and after the gasification process. The time and methylamine solution ratios strongly depend on the system configuration. In this sense, the reactants concentration and spatial configuration, modifies the diffusion rate to the system, affecting the final viscous solution. In our system, incorporation of 5 mol/mol of perovskite takes around 12 hours, while the incorporation of 10 mol/mol takes around 7 days. The incorporation rate follows a logarithmic tendency. Finally, ACN was added dropwise to the solution until have a 32% wt solution.

2.2.3. n-i-p perovskite solar cell fabrication

Devices were fabricated on ITO coated glass (Naranjo). The substrates were washed with neutral soap and sequentially sonicated in DI water, acetone and isopropanol. Then, they were treated with ultraviolet ozone for 5 min. The SnO_2 was fabricated in two-steps. First, a solution 0.048M $SnCl_2{\cdot}2H_2O$ in isopropanol was spin coated at 3000 rpm with an acceleration of 1000rpm for 30 s. Afterward, the substrates were annealed at 180°C for 1h. In the next step, the substrates were submerged at 70°C for 3 h in a chemical bath composed of 3.75g of urea, 62.5 μL of 3-mercaptopropionic acid, 3.75 mL of hydrogen chloride, 675 mg of $SnCl_2{\cdot}2H_2O$ and 250 mL of deionized water. Then, substrates were washed with deionized water, annealed at 180 °C for 1 h, and underwent UV-ozone treatment for 15 min. For the perovskite layer, 40 μL of precursor solution was deposited by spin-coating at 3000 rpm for 30 s. The films were then annealed at 120°C for 30 min. For the hole-transporting material, a solution of 70 mM of Spiro-OMeTAD in chlorobenzene and doped using 4-tert-butylpyridine and Li-TFSI in acetonitrile at a molar ratio of Spiro:Li-TFSI:TBP of 1:0.5:3.3 was used. Then, the solution was spin-coated at 4000 rpm for 20 s. Finally, to complete the devices, 80 nm of gold electrodes were thermally evaporated under vacuum ($\approx 10^{-6}$ mbar) at a deposition rate around 0.1 nm s^{-1}.

2.2.4. p-i-n perovskite solar cell fabrication

Patterned ITO substrates were washed sequentially in 2% of Mucasol solution in water, acetone and isopropanol, in an ultrasonic bath for 15 min. After that, UV treatment for 15 min was performed just before the HTL fabrication. All the deposition steps were conducted in a nitrogen atmosphere. After, 100 μL of SAM 2PACz solution (3 mg/10 mL absolute ethanol) were spin-coated at 3000 rpm for 30 s on a closed spin-coater. Annealing at 100°C for 10 min were performed. The perovskite solution was fabricated following the procedure reported by

Ramirez et al[118]. Here, 558 mg PbI_2, 152 mg $PbBr_2$, 232 mg FAI, and 72 mg CsI where mixed with 1 mL of DMF and 0.5 mL of DMSO. 100 μL of the precursor were dripped onto the SAM covered substrates and spread over the substate before the spinning program (5 s acceleration to 3500, 35s steady at 4000 rpm). Antisolvent chlorobenzene was added 5 s before the end of the program. Further, the perovskite was annealed at 100°C for 20 min. For the ETL, 23 nm of C60 were thermally evaporated with a rate of 0.1 Å/s. After that, 20nm of SnO_2 processed on top at a substrate temperature of 80°C via atomic layer deposition (ALD, Arradiance GEMStar) to form a buffer layer. SnO_2 precursors were tetrakis (dimethylamino) tin (IV)(TDMASn) and water. Finally, 100 nm of Cu was evaporated using a rate of 1 Å/s.

2.2.5. Characterization

X-ray diffraction patterns were measured using a Rigaku Miniflex600, in the range of 2θ=5° to 60° using Cu Kα (1.5408 Å) with a step size of 0.02° and a velocity of 5° per minute. Optical absorption was measured in the range of 400−800 nm using a Cary 100 Agilent spectrophotometer. FTIR measurements were collected in a range of 500 cm-1 and 4000cm-1 with a resolution of 4 cm-1, using ThermoFisher ATR iS50. AFM images were obtained in a MFP-3D infinity from Oxford instruments. For solar cell measurements, Keithley 4200SCS and solar simulator Oriel sol 3A were employed, calibrated to AM1.5 standard conditions using an oriel 91150 V reference cell.

2.3. Results and discussion

2.3.1. Formamidinium-based perovskites

Although the methods previously reported (Figure 2.1) yield high-quality $MAPbI_3$ films, they do not apply to mixed A-cation systems. Indeed, when a high amount of FA^+ replaces the MA^+ cations at the A-sites of the perovskites, the interaction of the solvation agent should be different. To have a better understanding of this process, mixed cation films $MA_{0.2}FA_{0.8}PbI_3$ were fabricated and characterized their crystalline structure by X-ray diffraction (XRD) as shown in Figure 2.2. Peeling, bubbling and dilution methods showed α-phase perovskite (at 2θ = 14.1°) with additional low angle peaks corresponding to non-perovskite phases (2H-δ phases/4H phases) [119] at 2θ around 11.6°; while degassing method not stabilize any amount of the perovskite phase. Additional unknown peaks at 2θ = 10.2°, 10.0°, and 9.2° are observed, those will be of importance in coming discussions. These results indicate that methods involving a viscous solution intermediate regarded as a metastable perovskite-MA precursor phase [120], are more prone to form active perovskite phases. Unlike the degassing method, the formation of the viscous solution intermediate allows the incorporation of several molecules of MA into the perovskite material. This observation, proven below, suggests that the amount of methylamine dissolving the perovskite precursor is a critical variable for the stabilization of the perovskite active phase.

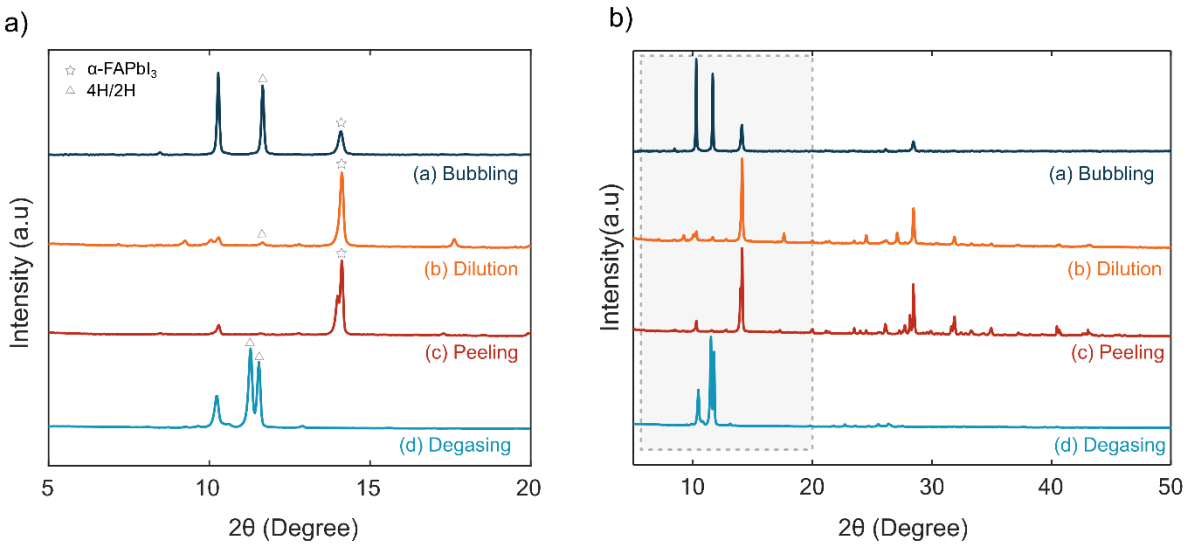

Figure 2.2. XRD diffractogram of the schematized methods using mixed cation composition $MA_{0.2}FA_{0.8}PbI_3$. a) Detailed XRD between 5° and 20°. b) Full XRD spectra

To demonstrate this observation, MA concentration was systematically studied in the dilution method, since this allowed more α-phase perovskite stabilization (Figure 2.2 line b). Perovskite films prepared from precursors with different mole amounts of MA were characterized by XRD, and UV-vis measurements in Figure 2.3. Clearly, increasing MA ratio in the solution directly increases the amount of α-phase at 14.1° (Figure 2.3 a) and reduces the low angle peaks ($2\theta < 10.2°$). The same trend is observed in the UV-vis measurement, where Figure 2.3b indicates that the presence of those unknown phases significantly affects the film absorption. In this behalf, a ratio of 10 mol MA per mol of perovskite powder could fully stabilize the α-perovskite phase, in agreement with a maximum absorption in the UVvis spectra (500-800nm).

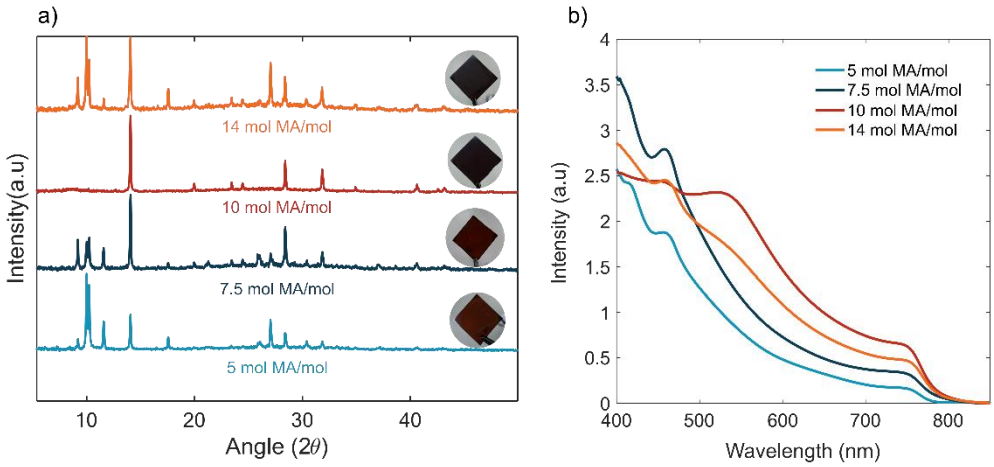

Figure 2.3. (a) XRD diffractogram at different ratios of methylamine mol per perovskite mol (b) UV-vis absorption spectra.

This observation highlights that precise control of the dissolvent has an enormous impact on the final perovskite film. However, MA ratios greater than 10 destabilized the precursor solution, leading to the formation of a pale yellowish precipitate as observed in Figure 2.4b. This behavior to was attributed to the consumption of MA molecules from the solution to form Pb-Alkylamide complexes, as previously reported by Kerner [103].

FTIR measurements of this compound indicate strong features of primary and secondary amines, as shown in Figure 2.4a. Additionally, XRD characterization shows different low peak angles under 10° (Figure 2.4b), supporting the Kerner reaction. Moreover, the crystallization during the spin-coating significantly changes depending on the methylamine ratio. For the case of low MA ratios, the crystallization is retarded (~ 20s – 30 s) and smooth films are obtained. In contrast, high MA ratios lead to rapid crystallization in seconds (~1s) similar to $MAPbI_3$ compositions processed in this solvent [108], [121].

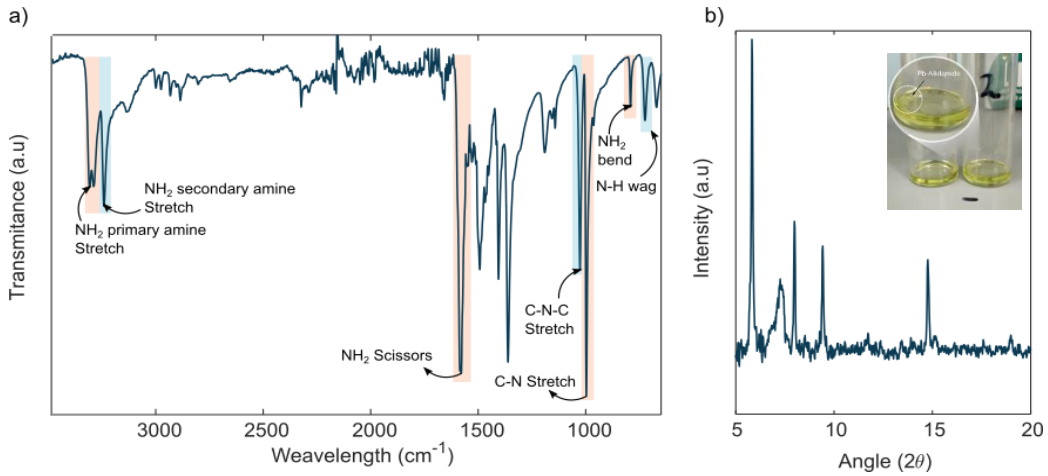

Figure 2.4. Characterization of Pb-Alkyl amide products at high MA amounts. a) FTIR characterization of the obtained precipitate. b) XRD of the precipitated and observed precipitate on the solution.

The unknown low angle peaks ($2\theta < 10.2°$) in the XRD data was assigned to a corner sharing structure of $FA_3(MA)PbI_5$. This non-perovskite structure is presumably formed for four reasons. First, it has a remarkable similitude with the reported crystallographic structure of the adduct phase $MA_3(DMF)PbI_5$ [122], where larger lattice parameters are expected due to the presence of larger FA^+ cations. Second, the presence of a 460 nm peak in the UVvis spectra (Figure 2.3b) has been previously attributed to the formation of PbI_5^{3-} species and assigned to a 1D formamidinium phase [123]. Thirdly, the ribbon-like structures observed in the AFM images (Figure 2.5) resemble similar shapes of low dimensional perovskite structures [122], [124], [125]. Finally, it has been reported that primary amines had greater donor numbers (40 – 50 kcal/mol) than conventional solvents DMF or DMSO (26.6 and 29.8 kcal/mol respectively). This suggests that the formation of adduct-like phase of MA molecules is rather possible [126], [127].

To disclose the molecular interaction of MA inside the mixed cation precursor, attenuated reflectance Fourier transform infrared spectroscopy (ATR-FTIR) was performed. Several spectral changes are observed upon increasing the MA ratio. As shown in Figure 2.6a, the peak at 1705 cm^{-1} is characteristic of the C=N stretch of FA^+ cation and gradually disappears upon the addition of MA, in correlation, a new peak emerges at 1665 cm^{-1}. This behavior is explained by the formation of hydrogen bonds between the methylamine and FA^+ cation. The interaction of MA with the amino group of formamidinium lead to an increased electron density around the nitrogen atom owing an inductive effect that modifies the polarity of the molecule [128]–[130]. As consequence, the double bond character is weakened, causing a shift of the C=N stretch to lower frequencies as it is observed. This trend is also observed when FAI is exposed to MA, indicating that PbI_6^{-4} is not involved in this new interaction. Also, the dipole interaction is supported by the Figure 2.6b, where the presence of a right-shift displacement in the vibrations of N-H stretches of MA (Shift from 3305cm^{-1} to 3283 cm^{-1} and 3365cm^{-1} to 3332cm^{-1}) indicates a dipole interaction of MA with the components in solutions and reinforced by the disappearance of NH_2 scissoring vibration at 1607cm^{-1}. Figure 2.6b also shows an additional small peak around 3500 cm^{-1} characteristic of O-H stretch of the ethanol diffused from methylamine solution. This incremental amount of ethanol did not significantly change the ratio between 1705cm^{-1} and 1665 cm^{-1} peaks and therefore did not have a substantial contribution to the phase stabilization. Finally, the role of ACN in the solvent was explored.

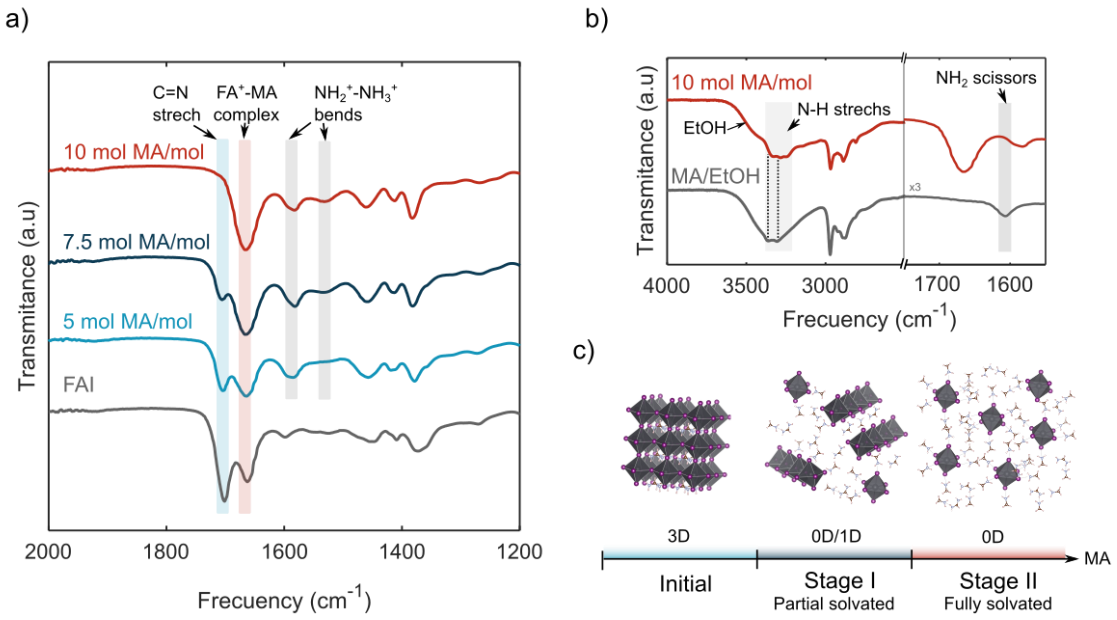

Figure 2.6. a) FTIR spectra of perovskite precursors with different MA ratios and FAI reference dissolved in methylamine. b) FTIR comparison between solution with 10 mol MA/mol powder and reference of methylamine in ethanol. C) Schematic representation of the stages involved in MA molecules solvation with mixed cation compositions.

Also, the results shows no peak displacements suggesting that acetonitrile acts only as a diluent in the precursor, in concordance with earlier observations by Jeong et al.[99].

To explain these results, a two-step mechanism is proposed, here, the MA interaction with theperovskite precursor (in this case, perovskite powder), lead to a viscous solution as summarized in Figure 2.6c. First, small amounts of physically adsorbed MA in the structure cause swelling, intercalating in the interplanar spaces and forming 1D $FAPbI_5$ ribbons, similar to the previous mechanism of Wu et al. [108]. Recrystallization at this point lead to the growth of those formamidinium phases, retaining the MA molecules inside and retarding the crystallization. Increasing the number of MA molecules allows a fully interaction with formamidinium cations, breaking the 1D phases in solution to form fully isolated 0D octahedral structures where the PbI_6^{-3} clusters are solvated by MA molecules, and all the FA cation complexed with at least one methylamine molecule. At this point, recrystallization favors the formation of 3D α-phase $FAPbI_3$ structures due to the increased cation disorder in the solution [131]. In addition, intermolecular interactions between MA molecules, leads to uniform evaporation that favors the rapid crystallization kinetics. Interestingly, this mechanism suggests that crystallization and phase stabilization is mediated by the interaction between the solvent (methylamine) and the site A cations (formamidinium). This observation is contrary to typical solvents (DMSO or DMF), where the iodoplumbate complexation solely determine the phase crystallization [132], [133]. Recently, similar observation of the formation of 1D phases upon MA exposure in $MAPbI_3$ perovskite has been reported [100], supporting the results.

So far, this work demonstrated that the stabilization of the perovskite phase in FA^+-rich compositions is possible. To validate this in a photovoltaic device, n-i-p solar cells were fabricated, and the power conversion efficiency (PCE) is illustrated in Figure 2.7, while the photovoltaic parameters are summarized in Table 2.1. With this morphology a maximum PCE of 11.1% was achieved for a concentration of 10mol. In agreement with a good quality perovskite α-phase as the active layer, that film can absorb light and transform it into charges, high photocurrents were obtained in precursors with high MA content; In contrast, lower photocurrents were obtained in the precursors with low MA content, since they have a large number of non-perovskite phases that are not photoactive and therefore cannot contribute to the generation of charges.[119] However, these devices showed higher open circuit voltage (Voc) due to their better film morphology. As shown in the AFM images of Figure 2.5, some pin-holes are present in the precursor with higher MA concentrations, reducing the V_{oc} and future optimization must obtain both, a stabilized perovskite phase (aim of this work) and high-quality morphology. This affectation on the V_{oc} hinders the future application of this precursor for the following photoelectrode integration.

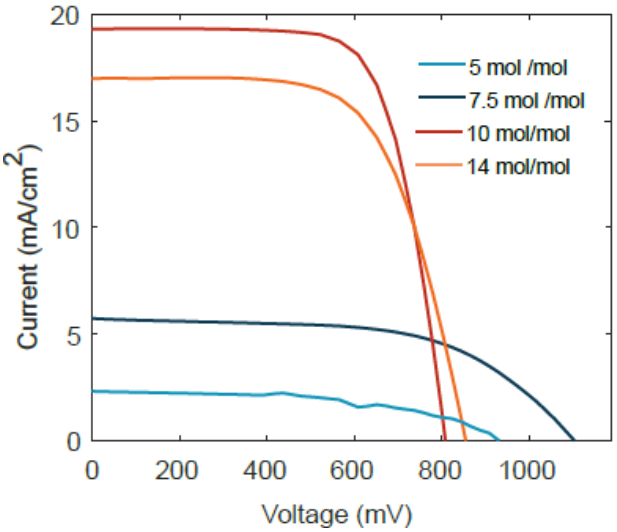

Figure 2.7. Reverse JV curves for the best-performing cells at different MA ratios on n-i-p architecture

Table 2.1. Photovoltaic parameters in dependence of the methylamine ratio on n-i-p perovskite architecture

	J_{sc}(mA/cm^2)	V_{oc}(mV)	FF(%)	PCE(%)
5 mol/mol	2.56±0.13 (2.56)	801.51±139.68 (951.80)	36.36±5.07 (43.82)	0.74±0.23 (1.07)
7.5 mol/mol	4.42±0.70 (5.73)	1059.10±21.10 (1102.03)	54.79±1.96 (57.98)	2.55±0.52 (3.66)
10 mol/mol	19.15±0.83 (19.79)	758.63±59.34 (801.56)	70.45±4.89 (69.98)	10.61±2.55 (11.10)
14 mol/mol	13.24±2.77 (15.61)	844.45±138.12 (973.23)	63.28±12.84(63.28)	7.62±2.53 (9.61)

In conclusion, this chapter demonstrated that for compositions with high FA^+, MA-based precursors are obtained only following routes that allow high contents of MA, like the viscous solution route. A detailed analysis of the precursor chemistry reveals that perovskites with high content of FA^+ tend to crystallize in 1D dimensional $FA_3(MA)PbI_5$ phases due the incomplete solvation of the PbI_6^- clusters. Here, the increasing the ratio of MA molecules in the precursor leads to full solvation, which is possible for the strong interaction between the FA^+ cations and MA molecules. Up to now, this vital role of MA ratio in the precursor has been overlooked because the traditional methods for the preparation of the MA based precursors do not control this variable. In contrast, the precursor with optimal MA ratio enabled rapid crystallization of 3D α-phase $MA_{0.2}FA_{0.8}PbI_3$ perovskite films, demonstrating great potential for upscaling to multication perovskite modules based on this precursor.

2.3.2. Beyond FA compositions using MA solvent.

Although the formamidinium cation has been proposed as the best candidate for stable perovskites, variation in the halide has suited a special part in the perovskite literature due the band gap tunability, with mayor applications in tandem devices and photoelectrodes [134]–[136]. Nonetheless, literature involving MA gas in this bromide composition is scarce. Zhao et al [28] using the healing method, publish that upon MA gas exposure, bromide films form a bleach state and return to a more crystalline configuration upon MA gas removal. Given the similarity with iodine compositional films, authors argue that halide did not affect the MA gas interaction. Years later, Nakita et al [121] found that following the bubbling method is not possible to obtain a stable precursor solution using $MAPbBr_3$. Although, modifying the lead source for HPbBr3, a stable precursor is obtained leading to devices with PCE of 7% and Voc of 1.52V.

To gain insights into this process, the $MAPbBr_3$ perovskite was probed using the earlier dilution method. First, perovskite bromide crystals were fabricated using the inverse temperature crystallization method as reported elsewhere[137]. With this method, millimeter size crystals were obtained as observed in figure 2.8a. Afterward, crystals were placed in MA gas overnight, obtaining a transparent and clear solution as observed in figure 2.8b. Finally, anhydrous acetonitrile was added dropwise to dilute the solution, but after contact with the viscous liquid, a white precipitate is formed as observed in figure 2.8c. This interesting observation opens a discussion about the role of the MA precursor. According to our previous observations with iodine compositions, acetonitrile does not affect the interaction and acts only as a diluent. Nonetheless, the behavior of bromide perovskite suggests that the stability of the solution is determinate by the diluent. Another interesting question emerges. Why the use of $HPbBr_3$ allows the stabilization of ACN/MA precursors as reported by Nakita? The role of $HPbX_3$ in perovskites has been controversial. According to Ke et al. [138], the $HPbX_3$ is not present. Instead, dimethylamine (DMA) molecules are formed in the $HPbX_3$ formation

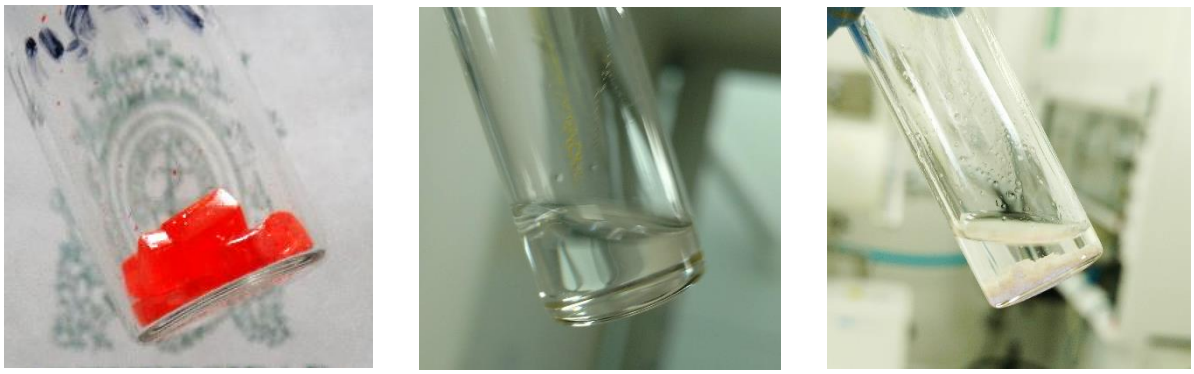

Figure 2.8: Transformation of $MAPbBr_3$ upon MA exposure. a) Pristine crystals. b) Crystals upon MA exposure. c) White precipitate upon acetonitrile dissolution.

reaction. If this is the case in the bromide counterpart, this reveals that cation modifications could alter the stability of precursor independently of the halide. Therefore, there is still a void in the literature on the role of MA in the case of different halides and their study will open an interesting discussion around the formation mechanism of such precursors. Although the deepening of this topic is out of the scope of this thesis, some follow-up experiments are proposed in the outlook section at the end of this chapter.

2.3.3. Highly efficient compositions with traditional precursors

Very long here, MA precursors remain as an interesting field with a vast range of research opportunities. Nonetheless, the efficiencies previously reported are not high and more efforts are required to obtain the desired photovoltaic performances reported elsewhere using conventional precursors. For this reason, aiming at the fabrication of a photoelectrochemical device, some literature methods were adopted to reproduce high-efficient devices on p-i-n architecture. The results are summarized in figure 2.9. In figure 2.9a, record devices with an efficiency of 19.45% are obtained. The perovskite used for device fabrication was the bication composition $Cs_{0.2}FA_{0.8}Pb\ (Br_{0.2}I_{0.8})_3$. Also, a superb reproducibility in this process was obtained with an average efficiency of 18.46%. Remarkably, these devices present an outstanding Voc of 1.15 V and a high fill factor of 78.6%, as observed in figure 2.9b. To corroborate the determined Jsc of the best device of 21.3 mA/cm^2, the external quantum efficiency (EQE) was measured showing an integrated current of 21.27mA/cm^2 , in perfect agreement with the best device performance. Finally, a maximum power point tracking of the devices was performed for 3 min. Here, to corroborate the real efficiency of the system, with

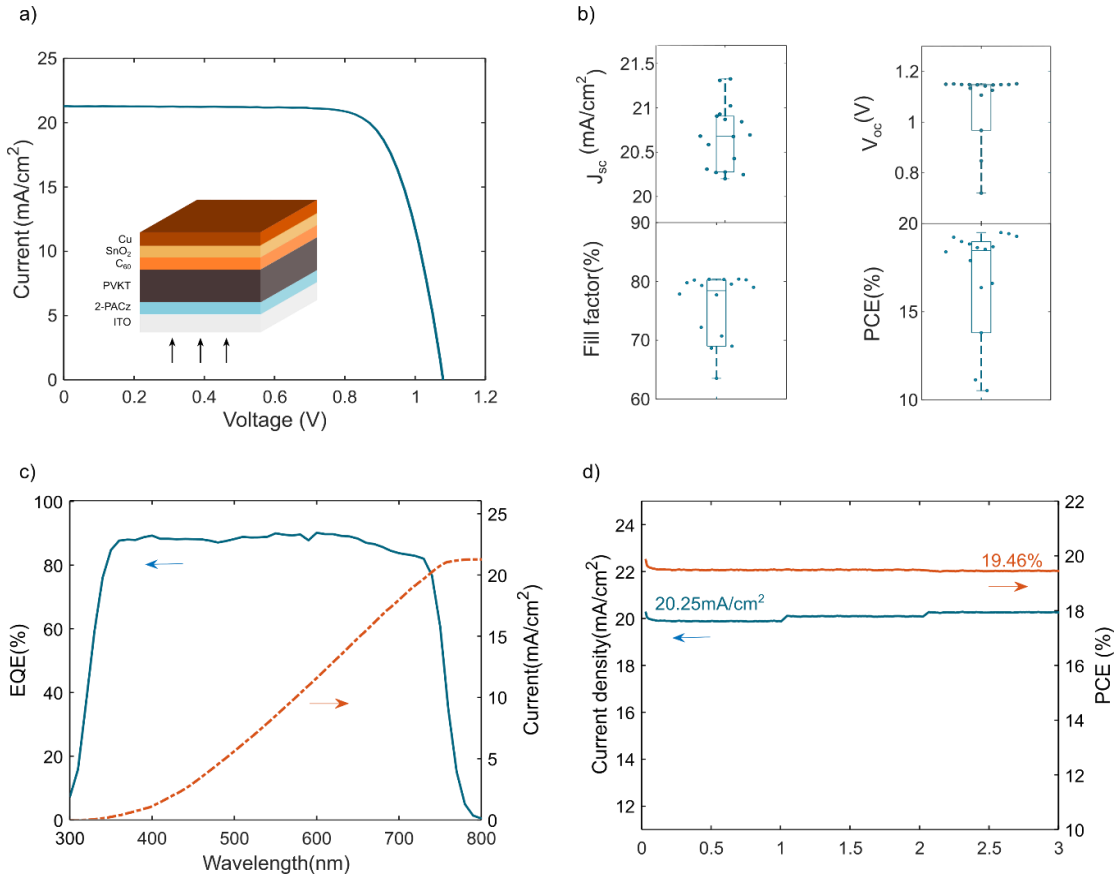

Figure 2.9: Photovoltaic performance of p-i-n devices. a) JV curve of the best device with PCE of 19.48%. b) Statistical distribution of the performance of 18 devices. c) EQE spectra and integrated photocurrent response. c) Maximum power point tracking for 3 minutes.

a steady-state efficiency of 19.45%. These results will be important in the final chapter of this thesis concerning the integration of the final device.

2.4. Conclusions

In this chapter, the methylamine was explored as a promising solvent to obtain scalable and reproducible devices. In this journey, the incorporation of this solvent on formamidinium-based perovskites is not straightforward because of the formation of 1D phases that hinder the photovoltaic performance. To ensure a fully 3D perovskite phase, proper tuning of the MA amount in the precursor is necessary to obtain a fully solvated state that allows a fast reconstruction of the perovskite active phase during crystallization. Furthermore, the role of the halide in this precursor was also explored. Here, depending on the halide, the role of the diluent inside the precursor varies, affecting the precursor stability. Finally, the fabrication of highly efficient devices using traditional solvent composition was performed, having a suitable benchmark for the fabrication of the photoelectrochemical devices.

2.5. Outlooks and recommendations of this section

Despite the advances realized upon here, several questions and issues are still unresolved, and the deepening in these experiments are out of the scope of this thesis. The summarized key experiments to follow up the advances on MA based precursors was presented in the followings.

a) **To accelerate MA incorporation is mandatory**: MA amount had an important role on the phase stabilization in FA perovskites. Nonetheless, the ideal amount of 10 mol/mol of MA takes around 1 week to incorporate under the studied conditions. Despite the previous methodology works as a controlled way to study the effect of the MA amount, their application is unviable if the reaction time takes a long time. For this reason, further studies about the kinetics of MA incorporation and methods to accelerate this process are mandatory to allow the application of this precursor for the fabrication of highly efficient devices.

b) **To improve the crystallization control:** According to the previous observations, the fast evaporation of MA in the spin-coating process, leads to huge voids that damage the final device performance. As suggestion, the next big step is to control the evaporation during the crystallization process to ensure a denser and pinhole-free structure. Here, studies focused on slot-die or blade-coating, could lead a more uniform evaporation and therefore, a more reproducible film. Also, the incorporation of additives that enhance the crystallization process could be a good choice for the implementation of this precursor.

c) **To incorporate Cs in the precursor:** According to the literature, the incorporation of CsI as additive allows the disappearance of non-active perovskite phases, like 4H/2H phases, also observed in our system as mentioned in figure 2.3. Unfortunately, CsI has very low solubility in acetonitrile, hence their application to our precursor is difficult. Therefore, studies focused on the dilution of CsI in suitable solvents or application of Cs from other precursors like $CsNO_3$ or $CsCO_3$ could be interesting for the continuation of the roadmap to obtain a triple cation composition, the benchmark composition to highly efficient devices.

d) **To modify the optical bandgap:** According to the figure 2b, the optical band gap appears at 790nm (1.58eV). According to literature, FA-based precursors have a lower band gap, between 1.45 and 1.51 eV. This observation is important because the matching of the bandgap is crucial for the obtention of highly efficient devices. That discrepancies in the bandgap could be because the incorporation of MA molecules into the structure lead to cation exchange process. According to this, the ratio of 0.8:0.2 is no longer true and the stability of the final film could be dramatically affected.

e) **Bromine incorporation:** As mentioned earlier, the incorporation of bromine into MA/ACN precursor is not straightforward. Modifying the cation for larger spacers like DMA could allow the stabilization of the bromine precursor. Also, the exploration of other solvents as diluent like THF, previously used in MA works [106] could help the stabilization of the bromide perovskite. This work is important because allows the fabrication of high-band gap perovskites, and the integration on triple cation perovskites.

Chapter 3:

Versatile layered double hydroxide NiFe catalyst

From materials characterization to deposition versatility

3.1. Introduccion

Layered double hydroxides (LDHs) have emerged as among the most promising candidates for water splitting catalysis due to their unique layered structures, providing a high electrocatalytic activity using low cost and abundant materials[139], [140]. In general, LDH materials are brucite-like lamellar crystals composed of positive host layers and charge-balancing interlayers following a general formula $[M^{+2}_{1-x} M^{+3}_{x} (OH)_2]^{x+} (A^{n-})_{x/n}$, in which M^{2+} and M^{3+} represent divalent and trivalent cations and A^{n-} is the charge-compensating interlayer anion [141]. Among this family, NiFe LDH catalyst have exhibit a great interest due their high catalytic activity, reporting among the lowest overpotentials in the family of earth abundant materials combined with high stability and activity for OER and HER reactions[139].

Multiple methods have been implemented to synthesize NiFe LDH powders or thin films. Some examples are hydrothermal/solvothermal synthesis[142], electrodeposition[34], coprecipitation[143], pulser laser deposition[144], among others. The hydrothermal/solvothermal route offers a control over the particle size and the crystal structure, as well as growth dynamics[139]. As a drawback, this technique uses high temperatures (~100°C-150°C) and demands long synthesis time (hours or days), limiting their implementation and scalability[145]. Electrodeposition offers low-cost, close connection, and electrical contact between the catalyst and the substrate, and also, properties like microstructure, composition and thickness could be finely tuned varying the bath composition, pH, temperature, and applied current density[139], [146]. Finally, coprecipitation offers a simple and versatile route to obtain highly active materials at different pH conditions. Also, the synthesis is fast, cheap and is usually performed at low temperature. Cheng et al [147], [148], reported the facile and scalable synthesis of NiFe LDH nanoparticles using this method, and assisting the obtention of the lamellar structures using ultrasonic exfoliation. With this method, they showed a high mass activity of 200 mA/mg^{-1} at an overpotential of 260 mV with a low Tafel slope of 21.2 mV/dec. Also, these nanostructures present a very high stability, remaining unchanged for more than 100h of continuous operation[148].

Once the material is synthesized, the method of application is crucial. A common method to probe this material is to apply the catalyst by drop-casting using a conductive binder to improve

the adhesion of the nanoparticles to the substrate. Nevertheless, this procedure reduces the electrocatalytic surface area, the mass activity and stability under harsh electrochemical activities[149]. For this reasons, self-supported electrocatalysts which are anchored directly on conductive substrates or form free-standing films have been gaining much attention recently. On this configuration, self-supported catalyst has the benefits of improving the mass transfer, the electron transport, and the surface area. Also increasing the simplicity of the process and reducing the final cost[141], [145], [149].

In this chapter, different deposition methods to fabricate binder-free NiFe LDH catalysts using scalable deposition methods was explored. First, the synthesis procedure of Chen [147] using the coprecipitation method was adopted, doing an extensive characterization of the produced NiFe LDH nanoparticles. Next, scalable spray coating technique was used as deposition method on ITO substrates evaluating their OER performance. Next, the use of printable conductive matrix by using Ni paste was used to evaluate the bifunctional activity of the catalyst. Finally, the implementation of the nanoparticles on Ni foam substrates was evaluated exploring different ultrasound exfoliation power to obtain highly efficient and stable bifunctional catalysts.

3.2. Experimental

3.2.1. NiFe LDH nanoparticles synthesis

The NiFe nanoparticles where produced by the technique of coprecipitation following an adapted protocol from Chen[147], 1.05 mol of Ni $(NO_3)_2{\cdot}6H_2O$ (305.32 mg) and 0.45 mol of $Fe(NO_3)_3 \cdot 9H_2O$ (181.8 mg) where added to 20 mL of NaOH 0.15 M under vigorous stirring. After 20 minutes of reaction, the solution was transferred to falcon tubes and centrifuge at 8000rpm for 5 minutes. Afterwards, the nanoparticles were washed using deionized water for 3 times repeating the centrifuge step. The collected precipitate where redispersed in 10 mL of deionized water to obtain the desired concentration. The nanoparticles exfoliation was

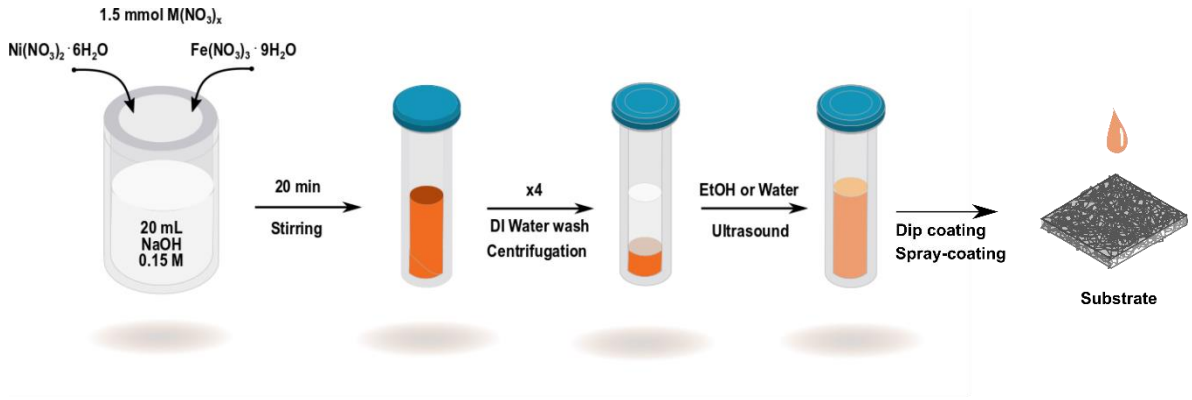

Figure 3.1. Graphical scheme of the synthesis route.

achieved by strong sonication on a Sonics vibracell model VCX130 varying the ultrasound amplitude to different values. The reached composition where 30% of Fe according to EDX measurements. The summarized process is represented in figure 3.1.

3.2.2. NiFe LDH nanoparticles deposition

In this work, two main methodologies for deposit the catalyst where used: Spray-coating and Dip-coating. First, substrates (Ni Foam or ITO substrates) where washed sequentially in ultrasonic bath of deionized water, isopropanol, and acetone. For the case of ITO substrates, ultraviolet/ozone (UVO) surface activation was used before the catalyst deposition. For the spray-coated samples, a quartz spray nozzle nebulizer (Meinhard,USA) was used. Here, a solution with concentration of 11 mg/mL were pumped at a rate of 1 mL/min and sprayed with a pressure of 0.5 MPa in the carrier gas. The nozzle was placed at 10 cm of the substrate and the film heated to 100°C to ensure the solvent evaporation. For the Ni-paste application, 1 mL of conductive Ni Paste (Voltex®, IQS SAS company) was applied over soda-lime glass. This paste was spread using a tip to ensure a coverage of the substrate. The substrates were left aside for 20 minutes at room temperature and then annealed at 60°C for 30 minutes. Afterward, the catalyst was added by drop-casting using 20 µl of catalyst solution over the dry substrates. Finally, for the dip-coated samples, 1 cm^2 of Ni Foam substrates where immersed in the catalyst solution, after 2 minutes in the solution, the catalyst was transferred to a hot plate at 100°C for 20 minutes.

3.2.3. Materials characterization

For the crystalline structure, X-ray diffraction patterns were performed using a Rigaku Miniflex600, in the range of 2θ=5° to 60° using Cu Kα (1.5408 Å) with a step size of 0.02° and a velocity of 5° per minute. For the case of powders, polylactic acid (PLA) holders were used to allow the characterization of low quantity of material. For films characterization, the material was deposited on soda lime glass. The transmission electron microscope (TEM) used was a Tecnai G2 F20 S-Twin TMP equipment, with a field emission source resolution of 0.1 nm in 200kV, maximum magnification in TEM 1.0 MX, GATAN camera US 1000XP-P. HRTEM (High resolution TEM) and SAED (Selected Area Electron Diffraction) images were analyzed using the Digital Micrograph software with the Difftools script[150]. FTIR spectra were collected in a range between 500 cm^{-1} and 4000cm^{-1} with resolution of 4 cm^{-1}, using ThermoFisher ATR iS50. AFM images were obtained in a MFP-3D infinity from Oxford instruments. Finally, the zeta potential and particles size were determined using a Zetasizer Pro with an incidence beam of 25°. For roughness characterization, Brukner perfilometer was used.

3.2.4. Electrochemical characterization

For the electrochemical characterization, electrodes were analyzed using a three-electrode configuration in an Autolab potenciostat. Pt wire was used as counter electrode and Ag/AgCl

and Hg/HgO as references electrodes depending on the used electrolyte, 1 M NaOH or 1M KOH respectively. All potential where calculated against the reversible hydrogen electrode (RHE) using the Nernst equation. Also, to verify the correct value of the reference electrode, hydrogen was bubbled in the solution in a platinum wire electrode to determine the potential difference against the hydrogen standard electrode. Linear sweep voltammetry was performed from 0.2 to 2.0 vs RHE at 2 mV/s for the anodic reaction and 0 to -0.5 vs RHE at 2 mV/s for the cathodic reaction. All electrochemical data were corrected with iR losses unless otherwise stated. For the series resistance determination, AC impedance spectroscopy were performed from 1000kHz to 0.1 Hz. Resistance value at real intersect were taken.

3.3. Results and discussion

3.3.1. Nanoparticles characterization

The targeted NiFe-LDH nanoparticles were fabricated using the coprecipitation method followed by ultrasonic exfoliation[147]. The obtained NiFe-LDH presents a plate-like morphology, which can be observed in the TEM image in Figure 3.2a. Also, uniformly distributed nanoparticles with a diameter of ~ 4nm was obtained, as shown in the inset image of Figure 3.2a. The hexagonal nano-shape commonly reported for of NiFe-LDH[151] is not

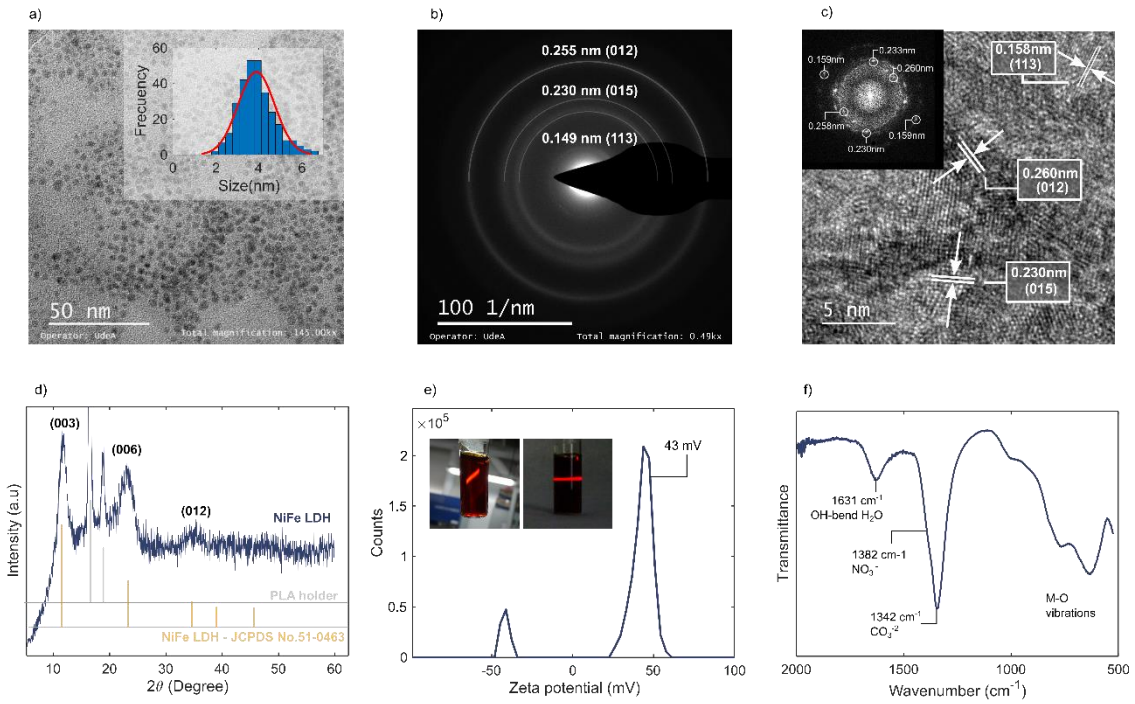

Figure 3.2. Morphological characterization of the NiFe LDH particles. a) TEM images of NiFe-LDH nanoparticles after exfoliation. B) SAED of NiFe LDH nanoparticles. C) HR-TEM of NiFe-LDH nanoparticles. D) XRD diffractogram C) Zeta potential and images of the obtained dispersion. D) FTIR of catalyst solution

observed, indicating a different growth path using the coprecipitation/exfoliation method. Figure 3.2b shows the SAED and Figure 3.2c the HR-TEM with the fast Fourier transform. Here, three main d-spacings are observed in both figures: 0.255nm, 0.230nm, 0.150nm. These are assigned to the planes (012), (015), and (113) of the NiFe LDH phases[152], [153]. The defined circles of the SAED indicate the low crystallinity of the nanoparticles. Interestingly, the plane (015) is the majority plane observed by FFT. This plane, along with the edge plane (012), has been associated with an incremental activity on the OER reaction[154]. Additionally, EDS measurement shows a Fe/Ni ratio of 0.7/0.3, preserving the stoichiometry from the reactants. Figure 3.2d shows the X-ray diffraction pattern of the NiFe-LDH powder. Here, peaks at 11.9°, 23.9°, and 35.6° are assigned to the planes (003), (006), and (012). These planes are also characteristic of the NiFe LDH phase (JCPDS spectra 51-0463).[155] Plane (015) is not observed in this analysis due the powder drying necessary for this test. Additional peak at 15.1° was assigned to the PLA holder used to the sample measurment. To further analyze the stability of the obtained colloidal suspension, zeta potential measurement was presented as observed in Figure 3.2e. Herein, the large electrostatic potential is related to the very good stability of the obtained dispersion after exfoliation. The quality of this suspension can be observed in the inset figures, where the Tyndall effect is observed, also indicating the colloidal nature of the obtained solution. This solution remains without visible precipitates for more than a month. Finally, to characterize the interplanar spacer of the NiFe-LDH nanoparticles, attenuated total reflectance fourier transform infrared (ATR-FTIR) measurement was performed. The result is observed in figure 3.2f. Strong peak at 1342cm^{-1} was assigned to the CO_3^- ion. Also, a shoulder at 1382 cm^{-1} is observed in Figure 3.2f, attributed to NO_3^- ions. The carbonate ion is very common to obtain during the LDH synthesis as probed by Hunter et al[144], due to the residual carbonates on water or CO_2 dilution during the fabrication procedure. Vibrations below 1000cm^{-1} have been attributed to vibrational modes of the double hydroxide metal M-O, M-O-M, O-M-O[156]. Herein, the synthetized NiFe LDH nanoparticles presumably follows the formula $[Ni^{+2}_{0.7}\, Fe^{+3}_{0.3}\, (OH)_2]^{0.3-}\, [(CO_3^{-2})_x\, (NO_3^-)_{1-x}]_{0.15}$, as conventionally reported stoichiometry for NiFe LDH nanoparticles.

3.3.2. Deposition of NiFe-LDH Catalyst: Spray coating method over ITO substrates

After obtaining a stable colloidal solution, the question on how to implement the nanoparticles in a functional device is crucial. Spray coating has very interesting features like direct (mask-free patterning), purely additive operation, compatibility with versatile materials and flexible substrates, low waste of materials, cost efficiency and scalability to large area manufacturing[157]. As an upgrade of spray-coating technique, Nebulizer spray coating allows a pinhole-free, highly adhesive, and good-quality film[158]. Therefore, in this section this technique was implemented to the previous synthetized catalyst. Two important variables were analyzed, the number of spray-coating steps and the solvent of the ink. Other parameters remain constant like nozzle-to-substrate height, nozzle aperture, spray rate, substrate

temperature and time of the coating cycle. Please refer to the experimental section to more details of the spray-coating process.

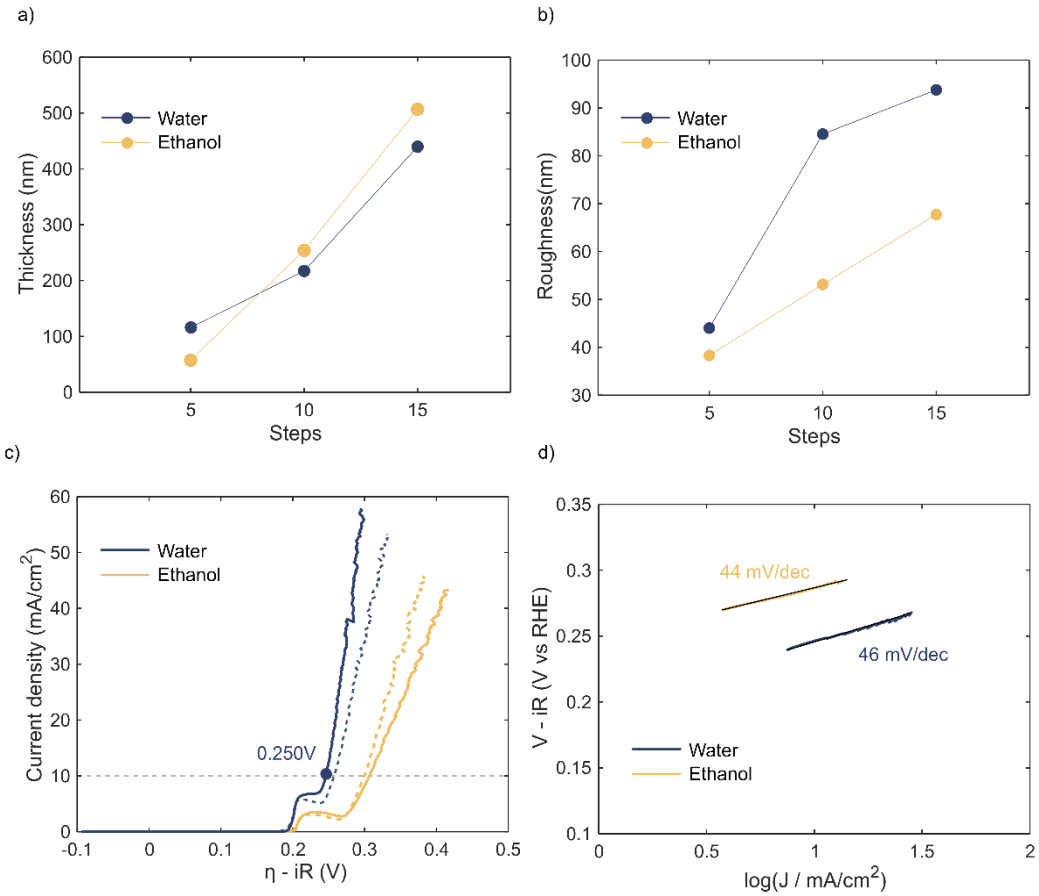

Figure 3.3. Spray-coating optimization and electrochemical performance. a - b) Variation of thickness and roughness in function of the number of spray coating steps in different solvents. c) Linear sweep voltammetry of the deposited catalyst at 1M NaOH (pH 13.3) measured against Ag/AgCl electrode and Pt wire counter-electrode. Continuous line represents 15 steps and dotted line 10 steps. d) Tafel slope extracted from linear sweep voltammetry.

Figure 3.3a-b shows the dependence of the solvent in the behavior of the thickness and roughness upon changes in the number of coating steps. Despite the solvent do not have an important effect on the film thickness, notable differences are observed in the roughness of the film. This effect is expected due to the different evaporation behavior on the substrate during the deposition step, nonetheless, further understanding of the deposition mechanism is required. An increased roughness implies higher surface area, beneficial for the electrochemical performance of the catalyst. Figure 3.3c shows the linear sweep voltammetry (LSV) in both solvents at 10 and 15 steps (Less steps were not evaluated due to the low homogeneity of the films). With the water solvent, overpotentials of 0.250V and 0.257 V are obtained at 15 and 10 steps, respectively. For ethanol, overpotentials of 0.290V and 0.283V at the same conditions were achieved. Note that the presented overpotential was measured at the

same thickness for both solvents, consequently, the catalyst charge in both cases is similar. Figure 3.3d shows the Tafel slope extracted from the best conditions in the LSV, noteworthy, both catalysts present a similar and low value in the Tafel slope. According to previous references, these low Tafel slopes are referred to the coverage of OH* species in the metal surface as the restraining step of the reaction at this low current density[20], [22], [159]. The similitude in the Tafel slope gives hints that the solvent or film morphology do not modify the kinetics of the reaction and the variations in the overpotential are due to the increase of active sites[148].

Despite the good performance of the obtained catalyst, due to the self-standing nature of the particles without binder, the catalyst presents a very poor adhesion to the ITO conductive substrate. After a long LSV operation, the mechanical stress produced by the bubbles, delaminates the film from the substrate, resulting in a complete failure in the stability of the material as shown in figure 3.4. Future efforts to improve the mechanical stability without affecting the electrochemical performance is required, some insights to improve this feature are given in the outlook section.

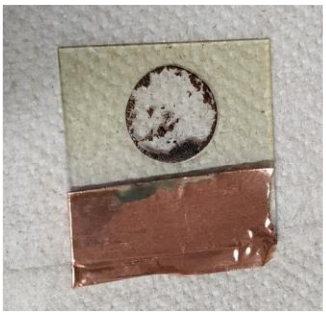

Figure 3.4. Appearance of the catalyst after LSV procedure before and after long term electrochemical activity.

3.3.3. Deposition of NiFe-LDH Catalyst: Dip-coating on Ni paste

In the previous section, the adhesion of the catalyst was a major issue for the spray-coated devices. Ni substrates have demonstrated great stability against OER and HER reactions in alkaline media, being the prime support for commercial alkaline electrolyzers[14]. Aiming to obtain scalable electrodes, the implementation of commercial nickel paste (Voltex®, IQS SAS company) as a conductive matrix for the NiFe LDH nanoparticle catalysts was explored. For detailed information on the paste application, please refer to the materials section. Figure 3.5 shows the anodic and cathodic performance of the catalyst using Ni paste as the conductive matrix. Without adding catalyst, the Ni paste presents a low catalytic performance with an estimated overpotential of 413mV at 20 mA/cm^2. The prominent peak around 1.43V (overpotential of 0.2V) is assigned to oxidation of $Ni(OH)_2$ to $Ni(OH)_3$. After adding the catalyst, a notable improvement in the performance was observed. Using a linear regression an overpotential of 265 mV at $10mA/cm^2$ was estimated. This value is slightly greater than the

ITO spray coating devices also in agreement with a larger Tafel slope as observed in Figure 3.5b.

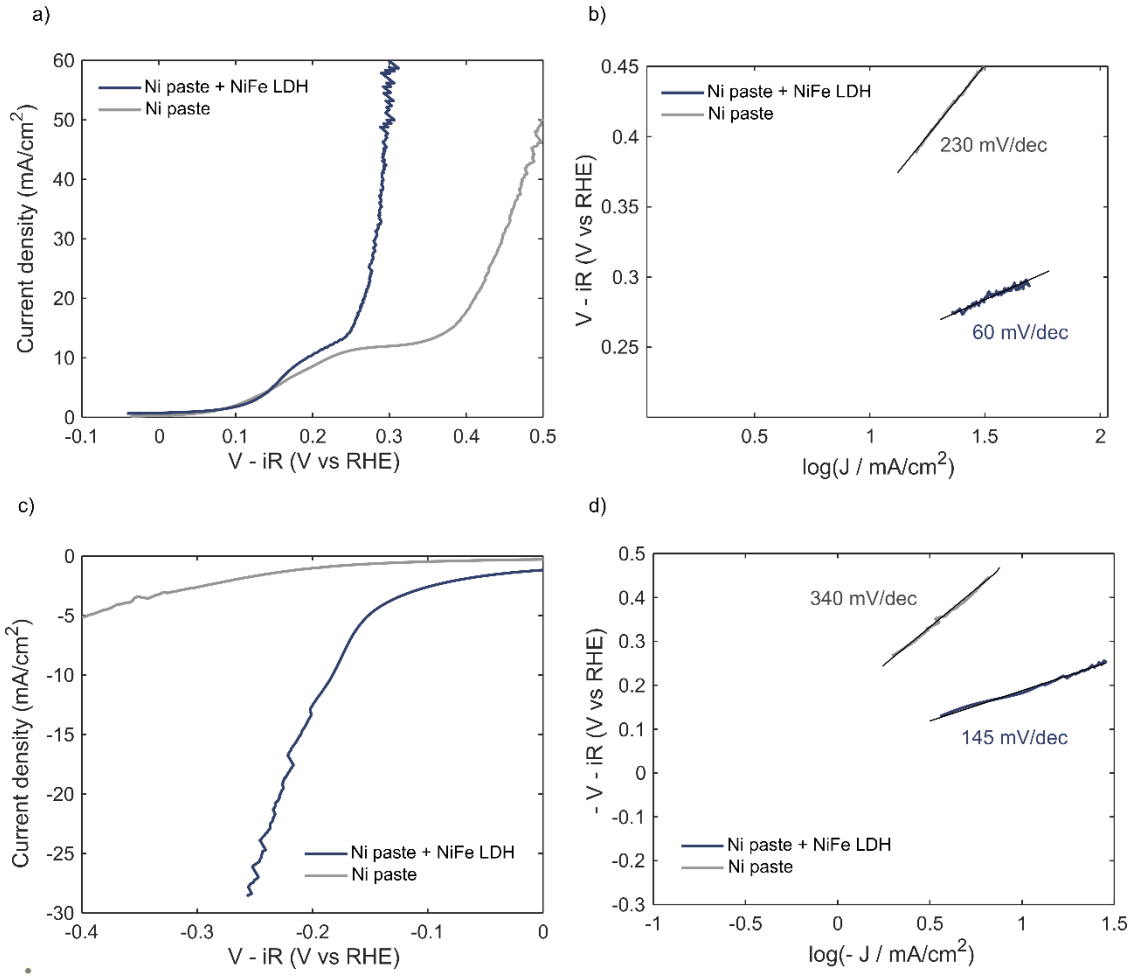

Figure 3.5. Electrochemical characterizations. All current densities and operating voltages were measured at 2mV/s in 1 M NaOH aqueous electrolyte against Ag/AgCl electrode with iR-compensation. Resistance of the substrates are ~ 8.2 Ω. a) Anodic LSV b) anodic Tafel slope c) Cathode LSV d) cathodic Tafel slope.

An enormous advantage of the Ni paste over the ITO is the stability under HER conditions. Figure 3.5 c-d shows the HER performance of the NiFe LDH catalyst. In these conditions, Ni paste activity is very low indicating the poor activity of only Ni substrates against HER. On the other hand, the catalyst presents a good overpotential of 189 mV at 10 mA/cm^2. Despite this is far from the state-of-the-art platinum counter electrode, which presents overpotentials lower than 100mV, these results are comparable with NiFe LDH reports. Further efforts in tuning the iron amount or compositional variations could drive to a more efficient catalyst as stated recently in various reports. Regarding the reaction mechanism, the large values of the Tafel slope (145 mV/dec) are hard to relate with the Volmer reaction mechanism (120mV/dec), suggesting an additional process that slow down the reaction and increase the overpotentials.

Detailed mechanistic studies could be made to determine the reaction path in these conditions, but they are out of the scope of this thesis.

Despite the adhesion of the catalyst was improved (No catalyst residues were observed in the solution after the LSV cycles), long-term evaluations were no possible due to the swelling of the Ni paste after the immersion in water, leading to the failure of the system after some minutes. Moreover, the consistency of the paste does not allow its application with controlled techniques like blade-coating or screen-printing. Therefore, manually drop coating was performed leading to variations in thickness and film conductivity, reducing dramatically the reproducibility of the system. As a result, comparison between different catalyst charge and drop coating conditions was not possible due to the scattered results when the Ni paste matrix was employed.

3.3.4. Deposition of NiFe-LDH Catalyst: Dip-coating on Ni foam

In this section, the influence of the ultrasound energy on the catalytic activity of the NiFe LDH nanoparticles was explored. A commercial Ni foam was used as supporting matrix, this has been stated as an excellent support for electrochemical applications. In this experiment, different wave amplitude percentage was used during the nanoparticle synthesis, varying from 40%, 70% and 100% for 30 minutes, equivalent to an energy of 12.56 kJ, 21.40 kJ and 50.613 kJ respectively.

To analyze the effect on the microstructure, TEM and AFM was employed as observed in Figure 3.6. At low power values (Figure 3.6a and 3.6d) the nanoparticles do not present a well-defined structure and clusters, or agglomerations are observed. On the other hand, in the maximum amplitude, clearly defined nanoparticles were observed with both techniques (Figure 3.6c and 3.6f). It is important to note that the preparation of the samples for both techniques are rather different, indicating that the similitude in the images denotes a clear effect of the power on the morphology of the nanoparticles. Another interesting feature emerges from the SAED images. All the images present the rings assigned to the edge planes (012), (015), and (113). Nonetheless, increasing the exfoliation power, fewer scatter circles are observed. This increment in the "crystallinity" of the sample is assigned to a decrease of nanoparticles agglomeration leading to a sample with preferential two-dimensional layered nanoparticles. These results suggest something important in the further discussion, larger sonication power produce more exfoliated nanoparticles and therefore, more active sites will be exposed. In contrast, less exfoliated nanoparticles lead to a more intimate contact between the nanoparticles due to the cluster morphology, being crucial for the charge transport even more in this binder-free system.

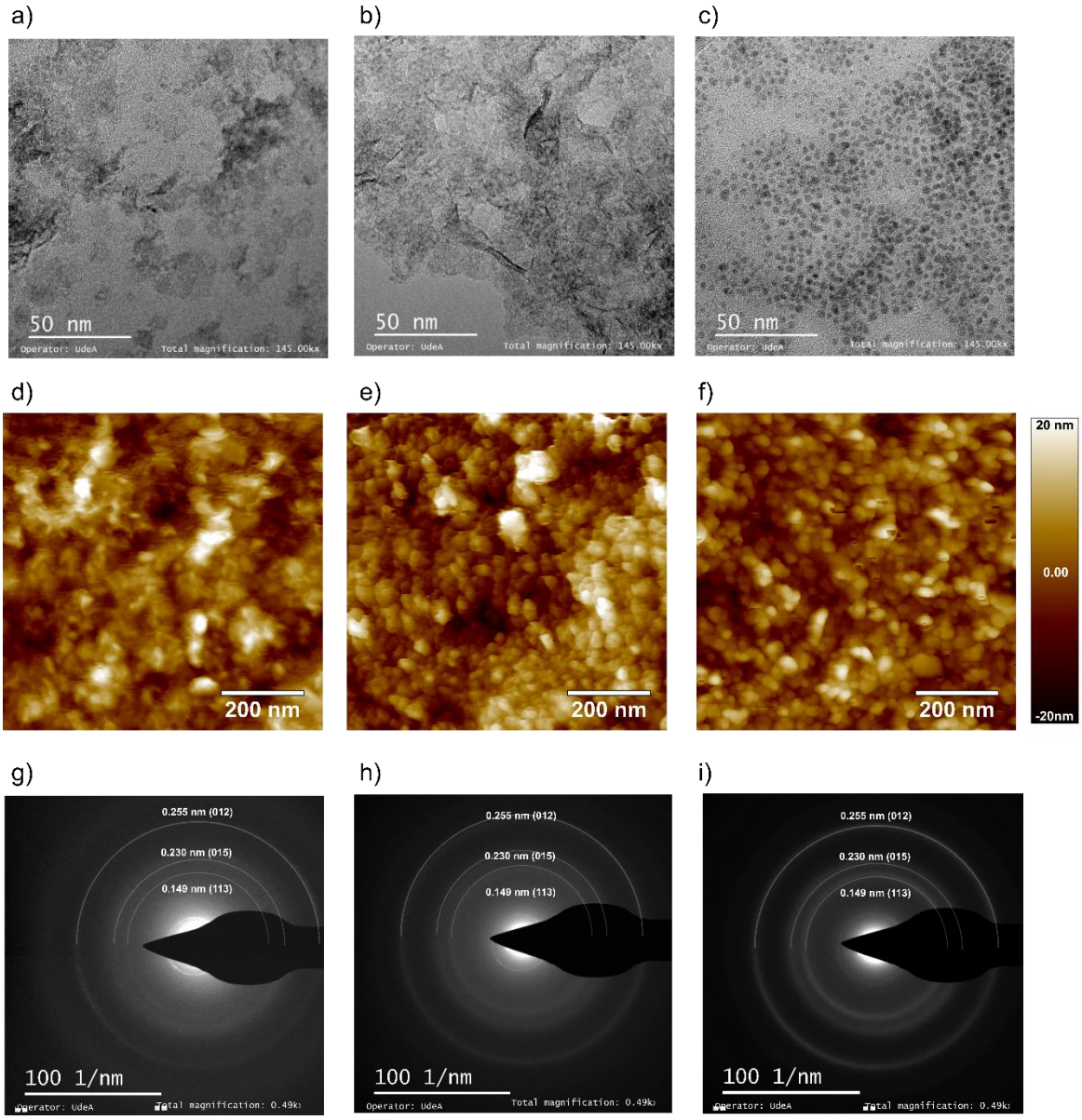

Figure 3.6. (a-c) TEM images at 40%, 70% and 100% power. (d-f) AFM images at 40%, 70% and 100% power. (g-i) SAED images of 40%, 70% and 100%.

To evaluate the electrochemical performance, the catalyst was deposited by immersing the foam in the catalyst solution for a minute to ensure full coverage of the foam. Three different immersion conditions were analyzed to validate the deposition method. The results of the electrochemical performance of this experimental design are shown in Figure 3.7. Figure 3.7a, summarizes the anodic performance in function of the exfoliation power and the number of immersions. Frequently, a larger number of immersions show better electrochemical activity by a difference of almost 20 mV at 30mA/cm^2. Here, a record overpotential of 243 mV at 30 mA/cm2 was achieved at 5 immersions and 70% of the power. Using linear regression to avoid the contributions of the Ni oxidation, an estimated overpotential of 232 mV at 10 mA/cm2 was calculated. To analyze in a particular condition, the effect of the power, we could consider the 5-immersion condition as shown in Figure 3.7b and 3.7c. Here, a record performance was obtained at 70% with a slightly better onset potential. Nonetheless, both conditions present approximately the same low Tafel slope, also equal to the previously calculated slope on the spray-coated technique. This indicates that under adequate deposition conditions, the charge transfer mechanism remains unvaried. On thicker catalyst layers, as expected for 5 immersions, the conduction between nanoparticles is harsher and their good interconnection is crucial. One hypothesis for the better performance at 70% is the balance between conductivity and active sites produced in the exfoliation, contributing to the maximization of the electrochemical

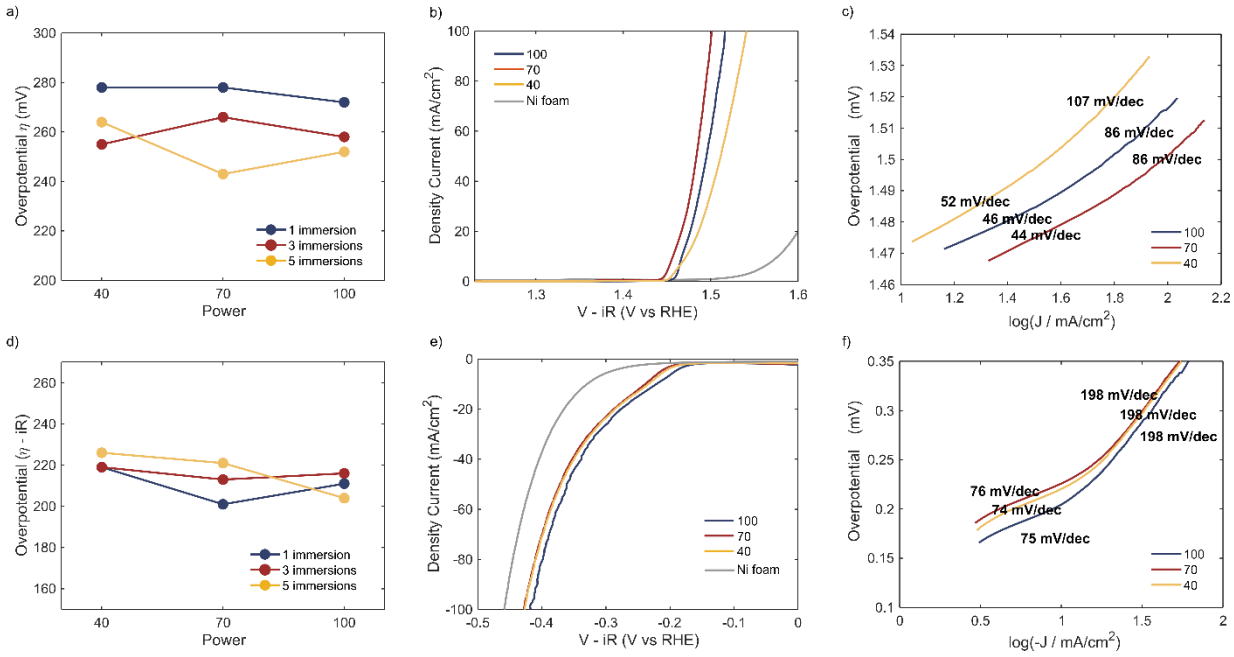

Figure 3.7. Electrochemical characterization~~s~~. All current densities and operating voltages were measured at 2mV/s in 1 M KOH aqueous electrolyte against Hg/HgO electrode with iR-compensation. Resistance of the substrates are ~ 2 Ω. a) Variation of the anodic overpotential at 30 mA/cm^2 in function of the power and the number of coating steps b) anodic LSV at 5 immersions. c) anodic Tafel slope at 5 immersions. d) Variation of the cathodic overpotential at 10 mA/cm^2 in function of the power and the number of coating steps. e) cathodic LSV at 5 immersions. d)cathodic Tafel slope at 5 immersions.

performance of the device. Further efforts to characterize this relationship are required as mentioned in the outlook of this chapter.

Figure 3.7b, presents the cathodic performance of the NiFe LDH supported in Ni foam. Here, no significant differences are observed between the immersion times. The 1 immersion system presents a good overpotential with a minimum value of 201mV at 10 mA/cm2. Analyzing again the condition at 5 immersions to compare the influence of the power, we notice that results do not reproduce the trends of the anodic counterpart. Here, best condition is obtained at 100% with an overpotential of 204 mV at 10 mA/cm^{2,} overpassing the other conditions by 20 mV. This observation is interesting because highlights that active sites for HER and OER are not necessary the same and focused optimization on each electrode is required to achieve the maximum performance of this catalysts. Moreover, following the previous trends of the anodic counterpart, the tafel slopes are equal irrespective of the used power. Nonetheless, comparing this results with the Ni paste experiments, a notorious reduction in the tafel slope is observed, suggesting an improvement in the charge transfer kinetics of the reaction. Further experiments to analyze how the supporting matrix affects the tafel slope are required to gain insights in these methods. Finally, is important to aware that possible improvements in the cathodic performance could be present due to the use of platinum as counterelectrode. As stated by Chen [160], the utilization of Pt as counterelectrode lead to a partial dissolution of the metal and subsequent deposition on the working electrode, improving the measured catalytic performance.

Finally, stability was another important parameter to analyze. Here chronopotentiometry measurements was performed to record the changes in potential on time at 10 mA/cm^2 for the 3 different power conditions at 1 immersion as presented in Figure 3.8. For the three conditions, a slightly increase in the potential during the first 5 hours is observed, followed by an almost steady voltage retaining 99% of the potential for 36 hours. This highlights the high stability of the synthetized catalyst. A drastically increase in the 40% condition is observed, while 70%

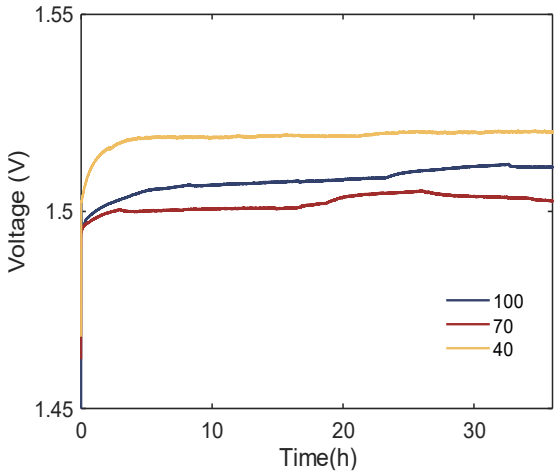

Figure 3.8. Chronopotentiometry measurement of NiFe LDH in Ni foam at different power sonication conditions

and 100% stabilize their potential much faster, probably related with the nanostructure configuration. On this condition, large clusters are present and therefore, more easily disconnected from the conductive matrix. After the experiment, an overpotential of 273 mV, 281 mV and 290 mV are observed for 70%, 100% and 40% respectively.

3.4. Conclusions

In conclusion, this chapter explore the fabrication of NiFe layered double hydroxide nanoparticles as a bifunctional catalyst for water splitting. Using the synthesis method of coprecipitation and ultrasonic exfoliation, stable colloidal nanoparticles was obtained with a diameter of around 8 nm exhibiting exposed edge planes. Different methods was evaluated to implement these nanoparticles as water splitting catalyst following the principle of large-scale application. First, a protocol was proposed to obtain highly efficient devices with an overpotential of 250mV using spray-coating technique. Secondly, Nickel paste was explored as a substrate to improve the mechanical adhesion of the nanoparticles. Despite interesting results in the overpotential the poor reproducibility hinders their implementation. Nonetheless, these experiments highlight the versatility of the HER reaction of this catalyst on Ni substrates. Finally, the catalyst deposition on the commercial-based Ni foam substrates was probed, obtaining results comparable with the literature with an overpotential of 232 mV for OER and 201 mV for HER. These results are comparable with previous reports on literature as shown in Table 3.1, suggesting that the versatility of the synthesized catalyst also reproduces the state-of-the-art performances. These advances suggest an important step towards versatile catalyst that could drive the water-splitting reaction and be compatible with large area deposition methods.

Table 3.1. Comparison of the current work with state-of-the-art results.

Synthesis	**Substrate**	**Coating method**	η_{OER}* **(mV)**	**Tafel (mV/dec)**	η_{HER}* **(mV)**	**Tafel (mV/dec)**	**Ref**
Coprecipitation	ITO	Spray coating	250	46	-	-	This work
Coprecipitation	Ni paste	Dip coating	265	60	186	145	This work
Coprecipitation	Ni foam	Dip coating	232	44	201	75	This work
Coprecipitation	GC	Dip coating	260	22	-	-	[147]
Hydrothermal	Ni foam	none	240	-	210	-	[77]
Hydrothermal	Ni foam	none	270	-	204	154	[161]
Hydrothermal	Ni foam	none	182	34	204	78	[162]
Hydrothermal	GC	Inkjet	270	31	-	-	[157]
Electrodeposition	Ni foam	-	205	82	175	127	[163]

* GC = Glassy carbon. None indicates that hydrothermal method deposits the catalyst directly on the substrate.

3.5. Outlooks and recommendations

- **To improve the adhesion to the substrate.** As stated in the chapter, adhesion was a major inconvenient in the performance of the studied catalyst, so its improvement is crucial for the implementation of these methodologies. In the spray coated technique, increasing the surface roughness of the substrate could favor the anchor of the nanoparticles. Also, the use of binders is interesting, but carefully control of the amount of binder is important to avoid the reduction on the electrocatalytic activity. Moreover, the use of composite materials like graphene or carbon nitrides could be interesting to enhance these systems.

- **To modify the substrates for bifunctional support using spray coating technique.** The use of ITO substrates on cathodic potentials are not possible given the corrosion of the Tin inside the structure. For this reason, the use of another planar substrate like Ni sheet or stainless-steel sheets could allow the validation of the activity of spray coated catalyst over the cathodic potentials.

- **To study the charge transfer between nanoparticles.** An interesting result of this work is the incremental activity on larger thickness. Previous reports states that NiFe LDH presents a very low conductivity [147], [161], [164] and so is counterintuitive that thicker films as much as over 500nm does not present a significant variation on the internal resistance as observed in measurements form figure 3.3. Therefore, a careful study to determine how is the charge transfer between the nanoparticles will be crucial for the design of this binder-free electrocatalyst.

- **To study mechanisms on the OER and HER reaction.** On the electrochemical systems, the determination of reaction mechanism is crucial for designing and improving the working electrodes. In this work, the Tafel slope was insufficient to predict the reaction mechanisms. Therefore, careful mechanistic studies must be developed to envision optimization roadmaps in these systems.

- **To modify the structural composition to improve OER and HER.** Despite the results are promising, the synthesized catalyst is still far from the best reported catalyst. Compositional modification toward ternary cations, spacer modifications or inset defects, could allow a reduction on the onset potential and incremental electrocatalytic activity.

Chapter 4:

Photoelectrochemical integration

Defining the goals for hybrid-perovskite incorporation

Introduction

Upon this point, this text has been working on the development of the two main components of photoelectrochemical devices: the perovskite absorber and the reaction catalyst. In this chapter, our attention will be focused on the integration of a photoelectrochemical device. Trying to integrate halide perovskites in a water environment is extremely challenging, considering that they degrade immediately upon water contact[165]–[167]. Therefore, despite their excellent semiconductor properties make them very interesting materials for photoelectrode applications, a very important question must be present in the development of this technology: Which are the advantages to immerse the perovskite absorber in water? The key claim previously exposed in the introduction is that immersion of the perovskite in water will be worth it if an electrolyte/semiconductor junction is formed, otherwise the option of PV+Electrolyzer is more reasonable.

Carefully examining the previous reports on perovskite absorbers as photoelectrodes, only the report by Kim[168] is compatible with this definition. Here suitable protection in acid environments is achieved using a bilayer of PCBM and atomic layer deposited (ALD) TiO_2, obtaining a very promising photocurrent of 10.5 mA/cm2 at 0 V and 0.5 suns of illumination. The authors also try to compare the relationship of this performance with a pure PV cell. Unfortunately, the sun simulator intensity in the PEC setup was half of the intensity used in the PV device, causing a reduction in the obtained current. Also, the amorphous nature of the ALD TiO_2 coating provokes a reduction on the device Voc, hindering the possible benefits derived from the electrolyte/semiconductor interface. Nonetheless, this result represents a very important milestone, demonstrating that perovskite semiconductor heterojunctions are capable to drive photoelectrochemical reactions. The other three common strategies to protect the perovskite from the environment (Metal encapsulation[81], Carbon encapsulation[85], [86], or resin sealing[169]) are more related to integrated PV+E devices than PEC devices. Here, the operation of the device is identical to a perovskite solar cell externally connected through a wire to the catalyst. Thus, the physics of carrier generation, charge separation, and catalysis remain unchanged.

In this chapter, the route to integrate perovskite semiconductors was investigated on photoelectrochemical devices. First, the integration of a PV+E using two perovskites solar cells connected in series to drive the overall water splitting reaction was explored, adding discussion about the role of tandem devices in this integration. Next, based on the insights previously exposed, the anodic reactions using an externally connected device on a three-electrode configuration were analyzed. Then, giving a step towards immersed devices, some concept demonstrations were given on the development of ALD protection layers for perovskite photoelectrodes integration. Finally, photocathodes were fabricated using highly degenerated semiconductors (IZO) to drive the hydrogen evolution reaction.

Materials and methods

4.2.1. Photovoltaic cell and catalyst

For the perovskite device, triple cation perovskite $Cs_{0.05}FA_{0.83}MA_{0.12}Pb(I_{0.6}Br_{0.3})_3$ solar cells were fabricated using the procedure described in chapter 2. The NiFe LDH was synthesized and deposited on Ni foam substrate following the procedures reported in chapter 3.

4.2.2. ALD deposition procedure and IZO sputtering

The thermal-assisted ALD for SnO_2 was performed using an Arradiance GEMstar. SnO_2 precursors were tetrakis (dimethylamino) tin (IV)(TDMASn) and water at 80°C. A total of 150 cycles were performed to obtain the desired thickness of 20 nm. For the TiO_2, a remote oxygen plasma ALD was performed using Picosun ALD equipment coupled with a plasma reactor. *tetrakis*(dimethylamino)titanium (TDMAT) was used as a precursor during the deposition process at 150°C. Here 160 cycles were performed to obtain a thickness of 20nm. Finally, IZO was sputtered in a Roth&Rau MicroSys200 PVD. The 2-inch ceramic target consisted of 90 wt% In_2O_3 and 10 wt% ZnO. At an RF power of 70 W, the cells oscillated under the target to have a uniform deposition[170].

4.2.3. Photoelectrochemical characterization

For the PV+E characterization, the Ni foam/NiFe LDH catalyst was immersed in a 1M KOH electrolyte. Keithley 2400 connected in a four points mode was used as a source measure unit. For the anodic evaluation, a three-electrode setup was used, here an Ag/AgCl reference electrode, Pt counter electrode, and 1 M KOH electrolyte were used. All potential was calculated against the reversible hydrogen electrode (RHE) using the Nernst equation. For this measurement also the Keithley 2400 was used. The chopped light graph was obtained manually, blocking the light from the sun simulator (Oriel 3A) on a 3-second interval. For AZO electrodes, a three-electrode setup using a phosphate buffer (K_2HPO_4| KH_2PO_4), Pt wire as a counter electrode, and Ag/AgCl as reference electrode were used. To calculate the solar-to-hydrogen efficiency (STH) the formula reported elsewhere was used[171].

$$STH(\%) = \frac{\eta_F \times V_{redox} \times I_{WE}}{P_{in}} \times 100$$

Were P_{in} is the incident power, I_{WE} the operating current, V_{redox} corresponding to the water redox potential equal to 1.23V and η_F the faradaic efficiency assumed as 1.

Results and discussion

4.3.1. PV + E integration for overall water splitting

Using the catalyst developed in chapter 3, the route of Luo[77] was followed to obtain an overall water splitting device. As shown in figure 4.1a, two perovskite cells are interconnected in series to drive the required potential in the reaction. Making use of this architecture, the device reaches a V_{oc} of 2.20V, Jsc of 11.30mA/cm2, and FF of 60.2, leading to a PCE of 14.9%. In the catalyst counterpart, the bifunctional catalyst Ni foam/Ni LDH was placed on a two-electrode set-up to record their potential dependence. At this configuration, a potential of 1.73V at 10 mA/cm^2 is required to drive the photoelectrochemical reaction, representing an electrochemical efficiency of 71%. From the intersection of the curve of the PV device and the two-electrode system is possible to estimate the solar-to-hydrogen (STH) efficiency of this PV+E system. Here an STH of 10.4% is calculated for the two-electrode system configuration as observed in Figure 4.1b. Figure 4.1c shows the bubbles of O_2 and H_2 generated without any bias applied to the device. On a detailed analysis of the integrated cells using the conventional perovskite with a 1.52eV bandgap, the room for improvement compared with Luo's work [77] is limited. On the best-performed devices for small cells, a maximum V_{oc} of 1.196V and 24.2 mA/cm^2 are obtained. Therefore, on a series of connected devices without interconnection losses, the perovskite solar cells will provide a maximum current of 12.1 mA/cm^2. Considering this current performance, a maximum STH of 14.76% could be obtained, significantly far from

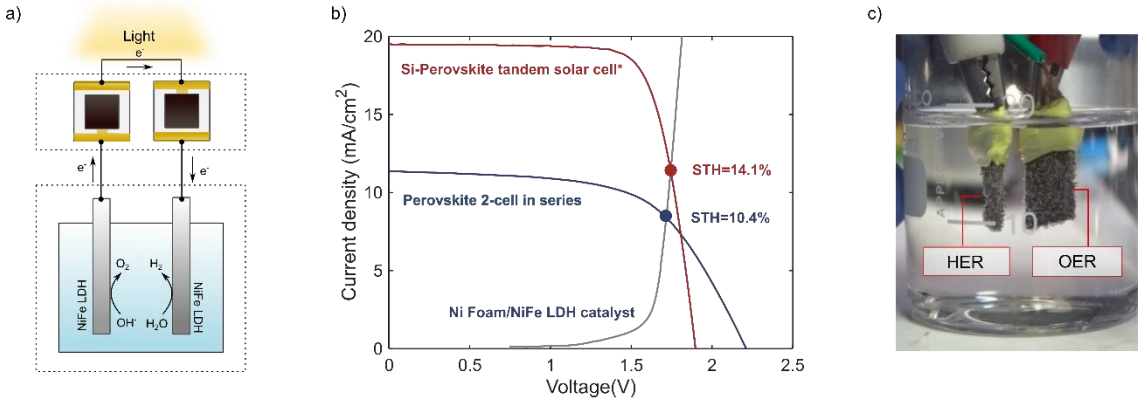

Figure 4.1. a) Schematics of the solar cell connection. b) PV+E figure of merit for overall water splitting. C) picture of the evolving bubbles without any applied bias.

the best-reported efficiencies for PV+E systems (>20%) [172]. On the other hand, explore the

option of multijunction devices opens a route for more efficient devices. Tandem devices have already demonstrated an outstanding performance of 29.5% using perovskite/silicon devices[173]. To outlook this potential, Figure 4.1 also presents a very efficient silicon/tandem device with a PCE of 27.9%. Here an STH of 14.1% will be obtained with the fabricated NiFe catalyst. Reducing the required cell potential to 1.5 V at 18 mA/cm^2 will lead to a potential STH of >23%. These results are feasible with the current technologies, projecting the perovskite semiconductor as an outstanding candidate for the efficient production of green hydrogen.

4.3.2. Literature ambiguity: PEC or integrated PV+E

A common misconception in literature reports using hybrid-perovskites is to call photoelectrodes to every device that is immersed. Here, to demonstrate the equivalence between what literature reports as PEC and an integrated PV+E device, a single perovskite device was connected to drive the anodic reaction following a three-electrode setup. The detailed scheme of the experiment is shown in Figure 4.2a. The device was placed outside the electrolyte and connected through a wire to the catalyst emulating the physical connection on an integrated device. Very interesting features can be extracted from Figure 4.2b. The maximum current obtained was 23.2 mA/cm^2 matching the short circuit current of the perovskite device. According to chapter 3, the used catalyst suffers a transition from Ni^{+2} to Ni^{+3} around 1.42V. Here this transition is observed around 0.35V, the difference between these two values is 1.07V, corresponding to the V_{oc} of the photovoltaic cell. Also, the solar cell act as a diode, therefore no current greater than 23.2 mA/cm^2 is observed even at potentials higher than 1.7V. This diode behavior is also observed at dark currents when no evolution reaction is occurring on larger potentials and the diode rectification at 0.3V vs RHE is observed. The spikes observed between 0.3V and 1V vs RHE could reveal interesting transient features on the perovskite absorber and the device dynamics, but detailed studies are required to explain

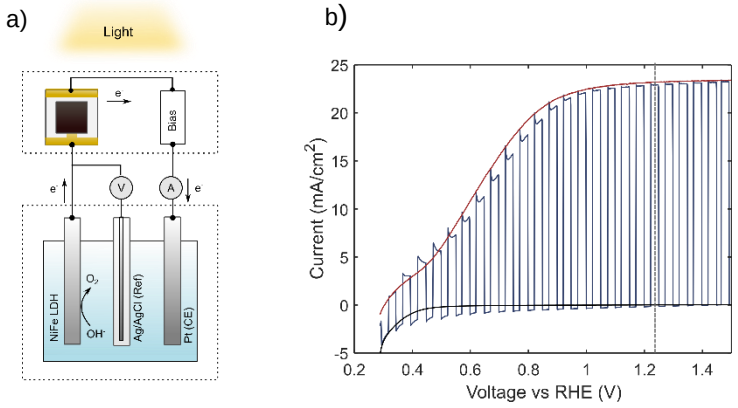

Figure 4.2. a) Scheme of integration for three-electrode measurement using external PV cell. b) Electrochemical response on 1M KOH. Red curve represents illumination, blue the performance under chopped light and black is the dark performance,

this observation. In conclusion, the reports of photocathodes or photoanodes in perovskite, are more related to integrated devices where the catalytic performance is restricted by the diode nature of the solar cell device, displacing the reaction potential to lower values and restricting the current to the values of the solar cell device. However, this measurement setup is extremely valuable. In case a real photoelectrode was fabricated, it provides a direct comparison between the PEC and PV+E systems.

4.3.3. Toward the development of PEC electrodes

4.3.3.1. ALD

As mentioned earlier, the ALD technique was the preferred method to successfully protect the hybrid perovskite and conserve the electrolyte/semiconductor interface. The Kim technique[168] uses a thermal-based ALD process. Despite it successfully protects the perovskite electrode, the low crystallinity of the TiO_2 layer limits the device performance, especially the photovoltage. In this section, to overcome this problem, two paths were followed: i) Substituting the transport layer by SnO_2 and ii) Modifying the deposition method by plasma ALD. Both strategies are described in detail in the following.

ALD SnO_2 has been used previously as a protection layer for photocathode applications[174]. Also, the SnO_2 has been applied extensively as a buffer layer on tandem devices, allowing the usage of sputtering techniques over the perovskite device[175], [176]. In chapter 2, the successful implementation of a perovskite solar cell using ALD SnO_2 was presented. Nonetheless, after exposing the layer to a drop of water, the molecules rapidly diffuse through the structure, leading to fast degradation of the perovskite film. The pristine film is observed in figure 4.3a and the resulting color after 2 minutes of exposure to the water droplets is shown in figure 4.3b. The low protection factor of the SnO_2, leading to the perovskite degradation, is probably for pinholes produced due to the presence of dust on the surface of the material or a

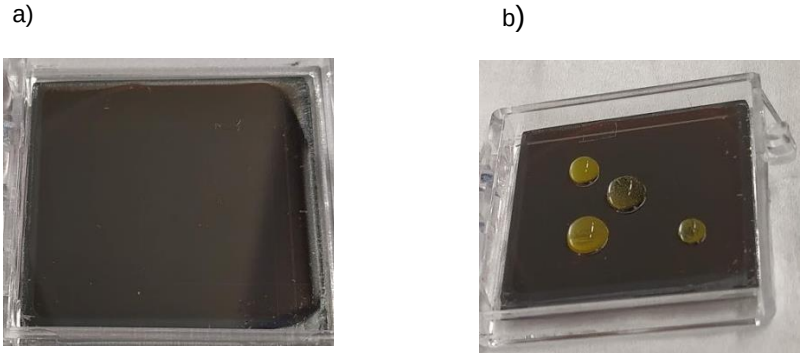

Figure 4.3. a) Pristine film after SnO_2 deposition process. B) Degradation of SnO_2 films after water droplet test

non 100% conformal coating. Further experiments to reveal the causes of the observed degradation are required to develop optimization pathways in this direction.

As a second approach for ALD protection, the study of TiO_2 by ALD was explored. As stated earlier, the thermal deposition of TiO_2 at low temperatures (<200°C) did not form a crystalline structure affecting considerably the device performance[177]. Moreover, the usage of H_2O as a ligand exchange unit noticeably affects the perovskite interface, requiring an additional component like PCBM to reduce this affectation[178]. As an alternative to thermal deposition, plasma-enhanced ALD (PE-ALD) provides a good option where heat treatment of substrates can be carried out near to room temperature, providing a uniform and conformal coating without destroying the substrates due to the thermal stress[179], [180]. In addition, impinging and highly reactive plasma species cause higher degrees of cross-linking within the growing thin film, making it more compact and denser[179]. Looking for the requirement of temperature, TiO_2 only forms crystalline structures at 150°C, therefore it was selected as the operating temperature in our study. Also, the remote oxygen plasma was determined as the best reductant condition for the deposition over perovskite semiconductors due to the reduced damage of this oxidant over the perovskite structure[181]. Please refer to the materials section for more consideration of the ALD deposition method.

Figure 4.4 shows the film after the ALD coating of 20nm of TiO_2. No visual changes are observed on the perovskite film after the ALD deposition process at 150°C denoting thermal stability of the material. Also, as a stability primary test, a water droplet was added to determine if any color change is observed. From perovskite material the transition to yellow PbI_2 occurs immediately after the water contact, therefore, it is an excellent mark for determining the stability of the film. In this experiment, a picture in Figure 4.4a shows the film after 20 minutes

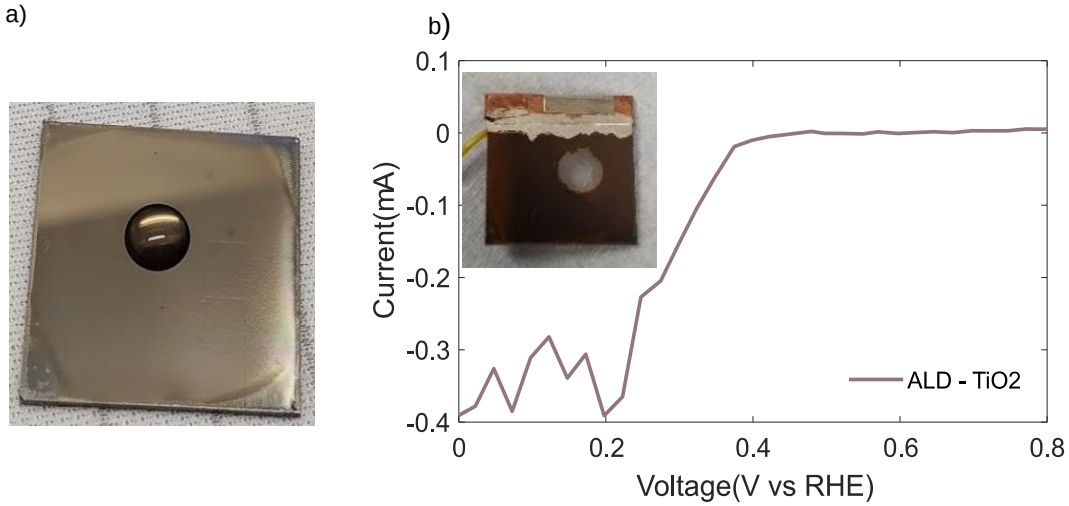

Figure 4.4. a) Perovskite film after 20 minutes of droplet test with TiO_2 as protection layer. B) Photoelectrochemical response under intermittent illumination using TiO_2 as protection layer

of droplet exposure. No notorious changes are observed at this time. This stability window successfully demonstrates the quality of the obtained film. As a second step, the photoelectrochemical performance of the device was measured. Here, no optical response is obtained after chopped illumination at 100W/cm^2 and AM 1.5. Further efforts to optimize the electronic properties alongside the protection capacity are required but are out of the scope of this thesis. Some insights to solve this problem are presented in the outlooks of this chapter. Finally, another interesting feature is observed in figure 4.4b. At potentials of 0.3V vs RHE, a strong reduction reaction is observed attributed to the lead reduction from Pb^{+2} to Pb^0. This highlights another huge challenge for perovskite as a photocathode. Photo-corrosion reactions are very prone to occur under the working potentials[172]. Because of this reaction, the complete damage of the material is produced as observed on the inset of figure 4.4b. Additional insights on the source of this photo corrosion phenomena will be of ultimate importance for the usage of perovskites photoelectrodes as stated in an excellent review by Samu and Janáky[172].

4.3.3.2.AZO protection layer

As a final strategy, the use of highly degenerated semiconductors like AZO or ITO, to protect the perovskite from the water environment was studied. These semiconductors have been extensively used for the fabrication of semitransparent perovskite solar cells or 4-terminal tandem solar cells. In these semiconductors, the Fermi level is very close to the conduction band, providing a high conductivity material and allowing their usage as a semitransparent electrode. These materials have been used as a protection layer for photoelectrode applications allowing a successful transport of charges[182], [183]. Here, taking advantage of the protection of SnO_2 towards sputtering coatings, the protection of the devices using sputtered Indium Zinc oxide (IZO) was studied. First, semitransparent perovskite solar cell devices were fabricated using a 300 nm thick electrode, obtaining an efficiency of 17.04% with a J_{sc} of 21.48 mA/cm2, V_{oc} of 1.10V, and FF of 0.725. These results confirm the adequate electronic coupling of the fabricated device.

Figure 4.5a presents the IZO substrate after 20-minute immersion without any applied bias. No degradation is observed in the material at this time. Subsequently, the photoelectrochemical response was analyzed on neutral pH (7.0 using a phosphate buffer solution) without any catalyst. The neutral pH was important due to the indium corrosion under basic or acid environments according to the Pourbaix diagram. The voltammetry results are shown in figure 4.5b. Some important results can be extracted from this graph. First, very low photocurrent from the device was observed, nonetheless, the presence of current response suggests some photocatalytic activity. It is worth highlighting that IZO does not present catalytic activity towards HER reaction, and therefore, the electronic response toward the chopped light might indicate photocatalytic effects from the heterojunction. Further characterization to analyze the produced reactants is required to validate the photoelectrochemical performance. Second, the

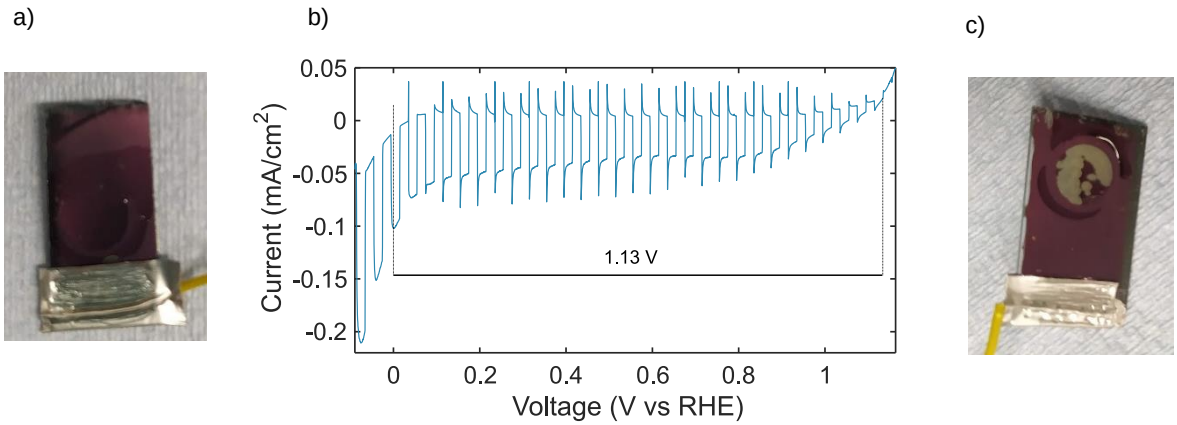

Figure 4.5. a) Perovskite film with AZO protection after 20 minutes of immersion in water b) Photoelectrochemical response under pH=7 (Phosphate buffer solution). c) Photoelectrochemical corrosion of the perovskite film.

photovoltage generated reassembly of the obtained potential from the PV device as observed in figure 4.5b, indicating a suitable match between the fabricated junctions. Finally, the corrosion at potentials near to 0 assigned to the reduction of lead is also observed, attributed to the dark current observed at this potential. This point is critical because when the potential in which this reaction occurs is reached, an immediate degradation of the device is observed as presented in figure 4.5c. One hypothesis for this behavior is that pinholes are present in the device. Therefore, when the devices are immersed, the decomposition towards PbI_2 occurs immediately on these nanometric spots. PbI_2 has very low solubility in water, so the water spread toward the film is reduced. Nonetheless, when the potential near to 0 is applied, the transition from Pb^{+2} to Pb^0 makes the water ingress very rapidly, also catalyzed by the induced potential, damaging the perovskite structure.

Conclusions

In this chapter, different pathways to integrate halide perovskites into photoelectrochemical devices were provided. As a guiding concept, the integration of perovskite-immersed devices will be worth it if an electrolyte/semiconductor junction is formed. Under this premise, two perovskites solar cells were connected in series with a bifunctional NiFe LDH catalyst following a PV+E configuration obtaining an STH of 10.4%. Then, following a PV+E configuration, the results of commonly named “photoelectrodes” in the literature are reproduced, demonstrating the equivalence on the physical phenomena involved in these configurations. Finally, the strategies to obtain an electrolyte/semiconductor junction with multiple heterojunction configurations were explored. Here, thermal ALD of SnO_2 is insufficient to protect the perovskite from direct water contact, but plasma ALD of TiO_2 is a good strategy to obtain suitable water protection, nonetheless, the electrical issues must be tuned to study the photoelectrochemical performance of these devices. Finally, the protection

of IZO, a highly degenerated semiconductor was studied as a protection option. Here, a photoelectrochemical response from the system was obtained but the lead corrosion hinders their application.

Outlooks and recommendations

- **Membrane implementation to more realistic PV+E systems:** To get closer the evaluated system toward a realistic environment, the addition of an adequate membrane is mandatory to allow the collection of gases and reduce losses that will be important on the scale-up of this technology. With the advances proposed in the perovskite and catalyst section, is expected that further enhancements on the reaction overpotential could be acquired, achieving higher electrochemical performances.

- **ALD optimization:** Despite the PE-ALD shows promising protection toward the water environment, the absence of photocurrent indicates a negligible electric contact between the materials. Improvement of the interface and careful evaluation of the film properties will be of utmost importance for the development of this protection strategy. Possible options are the prior deposition of electron transport layers like PCBM or C60, which successfully extract the charges from perovskite and protect the material during the growing steps. Finally, a thickness optimization must be performed to minimize the water permeation without affecting the film resistance and charge transport. Also, the option of the usage of inorganic perovskite materials like $CsPbBr_3$ will allow better thermal stability, allowing more temperature during the ALD cycles, improving the crystallinity and the density of the deposited film. Finally, detailed studies of the ALD growing cycles are important to ensure a fully conformal layer, avoiding pinholes or artifacts that limit the overall protection of the material.

- **Organic electrolytes for direct perovskite evaluation:** To further evaluate the semiconductor/electrolyte interface without the requirement of heterojunction protection, it is mandatory to modify the electrolyte for an organic media. Different organic electrolytes have been proven to be suitable to analyze the photoelectrochemical reactions of perovskites without notable degradation. This option will allow studying the semiconductor/electrolyte interface without the affectation of chemical degradation, opening the possibility to more detailed characterization in this field. Despite this option is not related to industrial applications, could open a window towards the understanding of this material and their possible benefits as a PEC semiconductor.

References

[1] S. J. Davis *et al.*, "Net-zero emissions energy systems," *Science.*, vol. 360, no. 6396, pp. 1–9, 2018, doi: 10.1126/science.aas9793.

[2] Hydrogen Council, "Hydrogen Scaling Up: A sustainable pathway for the global energy transition," pp. 2–80, 2017.

[3] IRENA, "Scenarios for the Energy Transition: Global experience and best practices," Abu Dhabi, 2020. [Online]. Available: https://www.irena.org/publications/2020/Sep/Scenarios-for-the-Energy-Transition-Global-experience-and-best-practices.

[4] IRENA, *World energy transition outlook. 1.5°C Pathway*, vol. 117. 2021.

[5] "Paris Agreement," 2015. https://unfccc.int/es/process-and-meetings/the-paris-agreement/el-acuerdo-de-paris.

[6] "Royal Society of chemistry," "Solar Fuels and Artificial Photosynthesis Science and innovation to change our future energy options," 2012.

[7] R. Kombargi, R. Hage, Y. Anouti, and S. Elborai, "The Dawn of Green Hydrogen: Maintaining the GCC's edge in a decarbonized world," 2020. [Online]. Available: https://www.iea.org/reports/the-future-of-hydrogen.

[8] International Energy Agency (IEA), "The Future of Hydrogen: Seizing today's opportunities," 2019. doi: 10.1787/1e0514c4-en.

[9] Hydrogen Council, "How hydrogen empowers the energy transition," 2017. [Online]. Available: http://hydrogencouncil.com.

[10] G. Glenk and S. Reichelstein, "Economics of converting renewable power to hydrogen," *Nat. Energy*, vol. 4, no. 1, pp. 216–219, 2019, doi: 10.1038/s41560-019-0326-1.

[11] Hydrogen Council, "Hydrogen Insights: A perspective on hydrogen investment, market development and cost competitiveness," 2021. [Online]. Available: http://hydrogencouncil.com.

[12] J. H. Kim, D. Hansora, P. Sharma, J.-W. Jang, and J. S. Lee, "Toward practical solar hydrogen production – an artificial photosynthetic leaf-to-farm challenge," *Chem. Soc. Rev.*, 2019, doi: 10.1039/C8CS00699G.

[13] S. van Renssen, "The hydrogen solution?," *Nat. Clim. Chang.*, vol. 10, no. 9, pp. 799–801, 2020, doi: 10.1038/s41558-020-0891-0.

[14] IRENA, "Green hydrogen cost reduction. Scaling up electrolysers to meet the 1.5°C climate goal," IRENA, Abu Dhabi, 2020. [Online]. Available: https://www.irena.org/-/media/Files/IRENA/Agency/Publication/2020/Dec/IRENA_Green_hydrogen_cost_2020.pdf.

[15] A. S. Joshi, I. Dincer, and B. V. Reddy, "Exergetic assessment of solar hydrogen production methods," *Int. J. Hydrogen Energy*, vol. 35, no. 10, pp. 4901–4908, 2010, doi: 10.1016/j.ijhydene.2009.09.067.

[16] F. Safari and I. Dincer, "A review and comparative evaluation of thermochemical water splitting cycles for hydrogen production," *Energy Convers. Manag.*, vol. 205, p. 112182, 2020, doi: 10.1016/j.enconman.2019.112182.

[17] "Heliogen." https://www.heliogen.com/.

[18] R. S. Poudyal *et al.*, "Hydrogen production using photobiological methods," *Compend. Hydrog. Energy*, vol. 10, no. 1, pp. 289–317, 2015, doi: 10.1016/b978-1-

78242-361-4.00010-8.
[19] H. Tributsch and L. Pohlmann, “Electron transfer: Classical approaches and new frontiers,” *Science.*, vol. 279, no. 5358, pp. 1891–1895, 1998, doi: 10.1126/science.279.5358.1891.
[20] J. Zhang *et al.*, “Advances in Thermodynamic-Kinetic Model for Analyzing the Oxygen Evolution Reaction,” *ACS Catal.*, vol. 10, no. 15, pp. 8597–8610, 2020, doi: 10.1021/acscatal.0c01906.
[21] V. Viswanathan, H. A. Hansen, J. Rossmeisl, and J. K. Nørskov, “Universality in oxygen reduction electrocatalysis on metal surfaces,” *ACS Catal.*, vol. 2, no. 8, pp. 1654–1660, 2012, doi: 10.1021/cs300227s.
[22] I. C. Man *et al.*, “Universality in Oxygen Evolution Electrocatalysis on Oxide Surfaces,” *ChemCatChem*, vol. 3, no. 7, pp. 1159–1165, 2011, doi: 10.1002/cctc.201000397.
[23] A. Govind Rajan, J. M. P. Martirez, and E. A. Carter, “Why Do We Use the Materials and Operating Conditions We Use for Heterogeneous (Photo)Electrochemical Water Splitting?,” *ACS Catal.*, vol. 10, no. 19, pp. 11177–11234, 2020, doi: 10.1021/acscatal.0c01862.
[24] B. Garlyyev, J. Fichtner, O. Piqué, O. Schneider, A. S. Bandarenka, and F. Calle-Vallejo, “Revealing the nature of active sites in electrocatalysis,” *Chem. Sci.*, vol. 10, no. 35, pp. 8060–8075, 2019, doi: 10.1039/c9sc02654a.
[25] O. Piqué, F. Illas, and F. Calle-Vallejo, “Designing water splitting catalysts using rules of thumb: Advantages, dangers and alternatives,” *Phys. Chem. Chem. Phys.*, vol. 22, no. 13, pp. 6797–6803, 2020, doi: 10.1039/d0cp00896f.
[26] X. Yu *et al.*, “Hydrogen Evolution Reaction in Alkaline Media: Alpha- or Beta-Nickel Hydroxide on the Surface of Platinum?,” *ACS Energy Lett.*, vol. 3, no. 1, pp. 237–244, 2018, doi: 10.1021/acsenergylett.7b01103.
[27] Y. Zheng, Y. Jiao, M. Jaroniec, and S. Z. Qiao, “Advancing the electrochemistry of the hydrogen- Evolution reaction through combining experiment,” *Angew. Chemie - Int. Ed.*, vol. 54, no. 1, pp. 52–65, 2015, doi: 10.1002/anie.201407031.
[28] J. O. M. Bockris, “Kinetics of activation controlled consecutive electrochemical reactions: Anodic evolution of oxygen,” *J. Chem. Phys.*, vol. 24, no. 4, pp. 817–827, 1956, doi: 10.1063/1.1742616.
[29] J. Song *et al.*, “A review on fundamentals for designing oxygen evolution electrocatalysts,” *Chem. Soc. Rev.*, vol. 49, no. 7, pp. 2196–2214, 2020, doi: 10.1039/c9cs00607a.
[30] M. Gong and H. Dai, “A mini review on NiFe-based materials as highly active oxygen evolution reaction electrocatalysts,” *Nanoresearch*, vol. 8, pp. 23–39, 2015, [Online]. Available: https://arxiv.org/ftp/arxiv/papers/1411/1411.4677.pdf.
[31] F. Dionigi, T. Reier, Z. Pawolek, M. Gliech, and P. Strasser, “Design Criteria, Operating Conditions, and Nickel-Iron Hydroxide Catalyst Materials for Selective Seawater Electrolysis,” *ChemSusChem*, vol. 9, no. 9, pp. 962–972, 2016, doi: 10.1002/cssc.201501581.
[32] C. C. L. McCrory, S. Jung, I. M. Ferrer, S. M. Chatman, J. C. Peters, and T. F. Jaramillo, “Benchmarking Hydrogen Evolving Reaction and Oxygen Evolving Reaction Electrocatalysts for Solar Water Splitting Devices,” *J. Am. Chem. Soc.*, vol. 137, no. 13, pp. 4347–4357, 2015, doi: 10.1021/ja510442p.

[33] F. Song *et al.*, “Transition Metal Oxides as Electrocatalysts for the Oxygen Evolution Reaction in Alkaline Solutions: An Application-Inspired Renaissance,” *J. Am. Chem. Soc.*, vol. 140, no. 25, pp. 7748–7759, 2018, doi: 10.1021/jacs.8b04546.
[34] A. M. P. Sakita, E. Vallés, R. Della Noce, and A. V. Benedetti, “Novel NiFe/NiFe-LDH composites as competitive catalysts for clean energy purposes,” *Appl. Surf. Sci.*, vol. 447, pp. 107–116, 2018, doi: 10.1016/j.apsusc.2018.03.235.
[35] Z. W. She, J. Kibsgaard, C. F. Dickens, I. Chorkendorff, J. K. Nørskov, and T. F. Jaramillo, “Combining theory and experiment in electrocatalysis: Insights into materials design,” *Science.*, vol. 355, no. 6321, pp. 1–12, 2017, doi: 10.1126/science.aad4998.
[36] J. A. Nelson, *Physics of solar cells*. London: Imperial Collage Press, 2003.
[37] P. Würfel and U. Würfel, *Physics of Solar Cells: From Basic Principles to Advanced Concepts*, 3th editio. Wiley, 2016.
[38] R. Van De Krol and M. Grätzel, *Photoelectrochemical Hydrogen Production*. Springer, 2012.
[39] W. K. Metzger, R. K. Ahrenkiel, J. Dashdorj, and D. J. Friedman, “Analysis of charge separation dynamics in a semiconductor junction,” *Phys. Rev. B - Condens. Matter Mater. Phys.*, vol. 71, no. 3, p. 035301, 2005, doi: 10.1103/PhysRevB.71.035301.
[40] L. Zhou *et al.*, “[ASAP] Cation Alloying Delocalizes Polarons in Lead Halide Perovskites,” *J. Phys. Chem. Lett.*, doi: 10.1021/acs.jpclett.9b01077.
[41] M. A. Green, “Photovoltaic principles,” *Phys. E Low-Dimensional Syst. Nanostructures*, vol. 14, no. 1–2, pp. 11–17, 2002, doi: 10.1016/S1386-9477(02)00354-5.
[42] “[ASAP] The Interplay of Contact Layers: How the Electron Transport Layer Influences Interfacial Recombination and Hole Extraction in Perovskite Solar Cells,” *J. Phys. Chem. Lett.*, doi: 10.1021/acs.jpclett.8b02824.
[43] T. T. Hien, N. D. Quang, C. Kim, and D. Kim, “Energy diagram analysis of photoelectrochemical water splitting process,” *Nano Energy*, vol. 57, pp. 660–669, 2019, doi: 10.1016/j.nanoen.2018.12.093.
[44] N. A. Kelly and T. L. Gibson, “Design and characterization of a robust photoelectrochemical device to generate hydrogen using solar water splitting,” *Int. J. Hydrogen Energy*, vol. 31, no. 12, pp. 1658–1673, 2006, doi: 10.1016/j.ijhydene.2005.12.014.
[45] C. Jacoboni, *Theory of Electron Transport in Semiconductors*. Springer, 2010.
[46] J. Chen and N.-G. Park, “Causes and Solutions of Recombination in Perovskite Solar Cells,” *Adv. Mater.*, doi: 10.1002/adma.201803019.
[47] F. Akira and H. Kenichi, “Electrochemical Photolysis of Water at a Semiconductor Electrode,” *Nature*, vol. 238, no. 5358, pp. 37–38, 1972.
[48] F. F. Abdi, L. Han, A. H. M. Smets, M. Zeman, B. Dam, and R. Van De Krol, “Efficient solar water splitting by enhanced charge separation in a bismuth vanadate-silicon tandem photoelectrode,” *Nat. Commun.*, vol. 4, pp. 1–7, 2013, doi: 10.1038/ncomms3195.
[49] A. Paracchino, V. Laporte, K. Sivula, M. Grätzel, and E. Thimsen, “Highly active oxide photocathode for photoelectrochemical water reduction,” *Nat. Mater.*, vol. 10, no. 6, pp. 456–461, 2011, doi: 10.1038/nmat3017.
[50] W. H. Cheng *et al.*, “Monolithic Photoelectrochemical Device for Direct Water

Splitting with 19% Efficiency," *ACS Energy Lett.*, vol. 3, no. 8, pp. 1795–1800, 2018, doi: 10.1021/acsenergylett.8b00920.
[51] Z. Wang, Z. Song, Y. Yan, S. (Frank) Liu, and D. Yang, "Perovskite—a Perfect Top Cell for Tandem Devices to Break the S–Q Limit," *Adv. Sci.*, vol. 6, no. 7, p. 1801704, 2019, doi: 10.1002/advs.201801704.
[52] S. E. Sofia, H. Wang, A. Bruno, J. L. Cruz-Campa, T. Buonassisi, and I. M. Peters, "Roadmap for cost-effective, commercially-viable perovskite silicon tandems for the current and future PV market," *Sustain. Energy Fuels*, vol. 4, no. 2, pp. 852–862, 2020, doi: 10.1039/c9se00948e.
[53] T. J. Jacobsson, V. Fjällström, M. Sahlberg, M. Edoff, and T. Edvinsson, "A monolithic device for solar water splitting based on series interconnected thin film absorbers reaching over 10% solar-to-hydrogen efficiency," *Energy Environ. Sci.*, vol. 6, no. 12, pp. 3676–3683, 2013, doi: 10.1039/c3ee42519c.
[54] B. Turan, J. P. Becker, F. Urbain, F. Finger, U. Rau, and S. Haas, "Upscaling of integrated photoelectrochemical water-splitting devices to large areas," *Nat. Commun.*, vol. 7, pp. 1–9, 2016, doi: 10.1038/ncomms12681.
[55] A. C. Nielander, M. R. Shaner, K. M. Papadantonakis, S. A. Francis, and N. S. Lewis, "A taxonomy for solar fuels generators," *Energy Environ. Sci.*, vol. 8, no. 1, pp. 16–25, 2015, doi: 10.1039/c4ee02251c.
[56] T. J. Jacobsson, "Photoelectrochemical water splitting: An idea heading towards obsolescence?," *Energy Environ. Sci.*, vol. 11, no. 8, pp. 1977–1979, 2018, doi: 10.1039/c8ee00772a.
[57] S. Chen, Y. Qi, C. Li, K. Domen, and F. Zhang, "Surface Strategies for Particulate Photocatalysts toward Artificial Photosynthesis," *Joule*, vol. 2, no. 11, pp. 2260–2288, 2018, doi: 10.1016/j.joule.2018.07.030.
[58] P. V. Kamat, "Photophysical, Photochemical and Photocatalytic aspects of the metal nanoparticles," *J. Phys. Chem. B*, vol. 106, pp. 7729–7744, 2002, doi: 10.1039/a901756i.
[59] Q. Wang *et al.*, "Scalable water splitting on particulate photocatalyst sheets with a solar-to-hydrogen energy conversion efficiency exceeding 1%," *Nat. Mater.*, vol. 15, no. 6, pp. 611–615, 2016, doi: 10.1038/nmat4589.
[60] A. Grimm, W. A. de Jong, and G. J. Kramer, "Renewable hydrogen production: A techno-economic comparison of photoelectrochemical cells and photovoltaic-electrolysis," *Int. J. Hydrogen Energy*, vol. 45, no. 43, pp. 22545–22555, 2020, doi: 10.1016/j.ijhydene.2020.06.092.
[61] R. van de Krol and B. A. Parkinson, "Perspectives on the photoelectrochemical storage of solar energy," *MRS Energy Sustain.*, vol. 4, no. 1, pp. 1–11, 2017, doi: 10.1557/mre.2017.15.
[62] O. Khaselev, A. Bansal, and J. A. Turner, "High-efficiency integrated multijunction photovoltaic/electrolysis systems for hydrogen production," *Int. J. Hydrogen Energy*, vol. 26, pp. 127–132, 2001, doi: 10.1021/acs.biomac.8b00819.
[63] G. Makrides, B. Zinsser, A. Phinikarides, M. Schubert, and G. E. Georghiou, "Temperature and thermal annealing effects on different photovoltaic technologies," *Renew. Energy*, vol. 43, no. June 2006, pp. 407–417, 2012, doi: 10.1016/j.renene.2011.11.046.
[64] S. Tembhurne, F. Nandjou, and S. Haussener, "A thermally synergistic photo-

electrochemical hydrogen generator operating under concentrated solar irradiation," *Nat. Energy*, vol. 4, no. 5, pp. 399–407, 2019, doi: 10.1038/s41560-019-0373-7.
[65] J. Bisquert, P. Cendula, L. Bertoluzzi, and S. Gimenez, "Energy diagram of semiconductor/electrolyte junctions," *J. Phys. Chem. Lett.*, vol. 5, no. 1, pp. 205–207, 2014, doi: 10.1021/jz402703d.
[66] H. Robatjazi *et al.*, "Plasmon-driven carbon–fluorine (C(sp 3)–F) bond activation with mechanistic insights into hot-carrier-mediated pathways," *Nat. Catal.*, vol. 3, no. 7, pp. 564–573, 2020, doi: 10.1038/s41929-020-0466-5.
[67] D. F. Swearer *et al.*, "Heterometallic antenna-reactor complexes for photocatalysis," *Proc. Natl. Acad. Sci. U. S. A.*, vol. 113, no. 32, pp. 8916–8920, 2016, doi: 10.1073/pnas.1609769113.
[68] L. Zhou *et al.*, "Quantifying hot carrier and thermal contributions in plasmonic photocatalysis," *Science.*, vol. 364, no. 6439, pp. 69–72, 2019, doi: 10.1126/science.aaw9545.
[69] M. Ahmed and I. Dincer, "A review on photoelectrochemical hydrogen production systems: Challenges and future directions," *Int. J. Hydrogen Energy*, vol. 44, no. 5, pp. 2474–2507, 2019, doi: 10.1016/j.ijhydene.2018.12.037.
[70] O. Hansen, I. Chorkendorff, D. Bae, B. Seger, and P. C. K. Vesborg, "Strategies for stable water splitting via protected photoelectrodes," *Chem. Soc. Rev.*, vol. 46, no. 7, pp. 1933–1954, 2017, doi: 10.1039/c6cs00918b.
[71] P. K. Nayak, S. Mahesh, H. J. Snaith, and D. Cahen, "Photovoltaic solar cell technologies: analysing the state of the art," *Nat. Rev. Mater.*, vol. 4, no. 4, pp. 269–285, 2019, doi: 10.1038/s41578-019-0097-0.
[72] A. Taloni, M. Vodret, G. Costantini, and S. Zapperi, "Size effects on the fracture of microscale and nanoscale materials," *Nature Reviews Materials*, vol. 3, no. 7. Springer US, pp. 211–224, 2018, doi: 10.1038/s41578-018-0029-4.
[73] A. Marchioro *et al.*, "Unravelling the mechanism of photoinduced charge transfer processes in lead iodide perovskite solar cells," *Nat. Photonics*, no. January, pp. 1–6, Jan. 2014, doi: 10.1038/nphoton.2013.374.
[74] M. I. H. Ansari, A. Qurashi, and M. K. Nazeeruddin, "Frontiers, opportunities, and challenges in perovskite solar cells: A critical review," *J. Photochem. Photobiol. C Photochem. Rev.*, vol. 35, pp. 1–24, 2018, doi: https://doi.org/10.1016/j.jphotochemrev.2017.11.002.
[75] N. Park and K. Zhu, "Scalable fabrication and coating methods for perovskite solar cells and solar modules," *Nat. Rev. Mater.*, vol. 5, pp. 333–350, 2020, doi: 10.1038/s41578-019-0176-2.
[76] C. Ran *et al.*, "Conjugated Organic Cations Enable Efficient Self-Healing FASnI3 Solar Cells," *Joule*, doi: 10.1016/j.joule.2019.08.023.
[77] J. Luo *et al.*, "Water photolysis at 12 . 3 % efficiency via perovskite photovoltaics and Earth-abundant catalysts," *Science.*, vol. 345, no. August, pp. 1593–1597, 2015, doi: 10.1126/science.1258307.
[78] J. Gao *et al.*, "Solar Water Splitting with Perovskite/Silicon Tandem Cell and TiC-Supported Pt Nanocluster Electrocatalyst," *Joule*, vol. 3, no. 12, pp. 2930–2941, 2019, doi: 10.1016/j.joule.2019.10.002.
[79] A. Sharma and F. J. Beck, "Quantifying and Comparing Fundamental Loss Mechanisms to Enable Solar-to-Hydrogen Conversion Efficiencies above 20% Using

Perovskite–Silicon Tandem Absorbers," *Adv. Energy Sustain. Res.*, vol. 2, no. 1, p. 2000039, 2021, doi: 10.1002/aesr.202000039.
[80] I. S. Kim, M. J. Pellin, and A. B. F. Martinson, "Acid-Compatible Halide Perovskite Photocathodes Utilizing Atomic Layer Deposited TiO2 for Solar-Driven Hydrogen Evolution," *ACS Energy Lett.*, 2019, doi: 10.1021/acsenergylett.8b01661.
[81] M. Crespo-Quesada, L. M. Pazos-Outón, J. Warnan, M. F. Kuehnel, R. H. Friend, and E. Reisner, "Metal-encapsulated organolead halide perovskite photocathode for solar-driven hydrogen evolution in water," *Nat. Commun.*, vol. 7, no. 1, pp. 6–12, 2016, doi: 10.1038/ncomms12555.
[82] J. Chung *et al.*, "Impact of Electrode Materials on Process Environmental Stability of Efficient Perovskite Solar Cells," *Joule*, vol. 3, no. 8, pp. 1977–1985, 2019, doi: 10.1016/j.joule.2019.05.018.
[83] P. Da, M. Cha, L. Sun, Y. Wu, Z. S. Wang, and G. Zheng, "High-performance perovskite photoanode enabled by Ni passivation and catalysis," *Nano Lett.*, vol. 15, no. 5, pp. 3452–3457, 2015, doi: 10.1021/acs.nanolett.5b00788.
[84] J. H. Kim *et al.*, "Efficient and Stable Perovskite-Based Photocathode for Photoelectrochemical Hydrogen Production," *Adv. Funct. Mater.*, vol. 31, no. 4, p. 2008245, 2021, doi: 10.1002/adfm.202008277.
[85] I. Poli *et al.*, "Graphite-protected CsPbBr3 perovskite photoanodes functionalised with water oxidation catalyst for oxygen evolution in water," *Nat. Commun.*, vol. 10, no. 1, p. 2097, 2019, doi: 10.1038/s41467-019-10124-0.
[86] R. Tao, Z. Sun, F. Li, W. Fang, and L. Xu, "Achieving Organic Metal Halide Perovskite into Conventional Photoelectrode: Outstanding Stability in Aqueous Solution and High-Efficient Photoelectrochemical Water Splitting," *ACS Appl. Energy Mater.*, p. acsaem.8b02072, 2019, doi: 10.1021/acsaem.8b02072.
[87] E. M. Tennyson, T. A. S. Doherty, and S. D. Stranks, "Heterogeneity at multiple length scales in halide perovskite semiconductors," *Nat. Rev. Mater.*, vol. 4, no. 9, pp. 573–587, 2019, doi: 10.1038/s41578-019-0125-0.
[88] S. Brittman, G. W. P. Adhyaksa, and E. C. Garnett, "The expanding world of hybrid perovskites: Materials properties and emerging applications," *MRS Communications*, vol. 5, no. 1. pp. 7–26, 2015, doi: 10.1557/mrc.2015.6.
[89] National Renewable Energy Laboratory (NREL), "Research Cell Efficiency Records Chart," *National Center for Photovoltaics*, 2020. https://www.nrel.gov/pv/cell-efficiency.html (accessed Aug. 24, 2020).
[90] T. Jesper Jacobsson *et al.*, "The Perovskite Database Project: Releasing the Power of the Crowd with FAIR Data Management," *Nat. Energy*.
[91] N. J. Jeon, J. H. Noh, Y. C. Kim, W. S. Yang, S. Ryu, and S. Il Seok, "Solvent engineering for high-performance inorganic-organic hybrid perovskite solar cells," *Nat. Mater.*, vol. 13, no. 9, pp. 897–903, 2014, doi: 10.1038/nmat4014.
[92] A. Babayigit, J. D'Haen, H. G. Boyen, and B. Conings, "Gas Quenching for Perovskite Thin Film Deposition," *Joule*, vol. 2, no. 7, pp. 1205–1209, 2018, doi: 10.1016/j.joule.2018.06.009.
[93] B. Conings *et al.*, "A Universal Deposition Protocol for Planar Heterojunction Solar Cells with High Efficiency Based on Hybrid Lead Halide Perovskite Families," *Adv. Mater.*, vol. 28, no. 48, pp. 10701–10709, 2016, doi: 10.1002/adma.201603747.
[94] X. Li *et al.*, "A vacuum flash-assisted solution process for high-efficiency large-area

perovskite solar cells," *Science.*, vol. 353, no. 6294, pp. 58–62, 2016, doi: 10.1126/science.aaf8060.
[95] S. Sánchez *et al.*, "Flash infrared annealing as a cost-effective and low environmental impact processing method for planar perovskite solar cells," *Mater. Today*, vol. 31, no. 31, pp. 39–46, 2019, doi: 10.1016/j.mattod.2019.04.021.
[96] B. Dou *et al.*, "Roll-to-Roll Printing of Perovskite Solar Cells," *ACS Energy Lett.*, vol. 3, no. 10, pp. 2558–2565, 2018, doi: 10.1021/acsenergylett.8b01556.
[97] E. Radicchi, E. Mosconi, F. Elisei, F. Nunzi, and F. De Angelis, "Understanding the Solution Chemistry of Lead Halide Perovskites Precursors," *ACS Appl. Energy Mater.*, vol. 2, no. 5, pp. 3400–3409, 2019, doi: 10.1021/acsaem.9b00206.
[98] D. Burkitt *et al.*, "Acetonitrile based single step slot-die compatible perovskite ink for flexible photovoltaics," *RSC Adv.*, vol. 9, no. 64, pp. 37415–37423, 2019, doi: 10.1039/c9ra06631d.
[99] D.-N. Jeong *et al.*, "Perovskite Cluster-Contained Solution for Scalable D-bar Coating Toward High Throughput Perovskite Solar Cells," *ACS Energy Lett.*, vol. 5, no. 4, pp. 1189–1195, 2019, doi: 10.1021/acsenergylett.9b00042.
[100] X. Huang *et al.*, "Methylamine-Dimer-Induced Phase Transition towards MAPbI3 Films and High-Efficiency Perovskite Solar Modules," *J. Am. Chem. Soc.*, vol. 142, no. 13, pp. 6149–6157, 2020, doi: 10.1021/jacs.9b13443.
[101] K. Wang *et al.*, "A Nonionic and Low-Entropic MA(MMA)nPbI3-Ink for Fast Crystallization of Perovskite Thin Films," *Joule*, vol. 4, no. 3, pp. 615–630, 2020, doi: 10.1016/j.joule.2020.01.004.
[102] A. J. Ramadan *et al.*, "Unravelling the Improved Electronic and Structural Properties of Methylammonium Lead Iodide Deposited from Acetonitrile," *Chem. Mater.*, vol. 30, no. 21, pp. 7737–7743, 2018, doi: 10.1021/acs.chemmater.8b03084.
[103] R. Kerner *et al.*, "Amine additive reactions induced by the soft Lewis acidity of Pb 2+ in halide perovskites. Part I: evidence for Pb–alkylamide formation," *J. Mater. Chem. C*, 2019, doi: 10.1039/c8tc04871a.
[104] J. A. Yang, T. Qin, L. Xie, K. Liao, T. Li, and F. Hao, "Methylamine-induced defect-healing and cationic substitution: A new method for low-defect perovskite thin films and solar cells," *J. Mater. Chem. C*, vol. 7, no. 35, pp. 10724–10742, 2019, doi: 10.1039/c9tc03490k.
[105] N. K. Noel *et al.*, "A low viscosity, low boiling point, clean solvent system for the rapid crystallisation of highly specular perovskite films," *Energy Environ. Sci.*, vol. 10, no. 1, pp. 145–152, 2017, doi: 10.1039/C6EE02373H.
[106] Q. Liu *et al.*, "A mixed solvent for rapid fabrication of large-area methylammonium lead iodide layers by one-step coating at room temperature," *J. Mater. Chem. A*, vol. 7, no. 31, pp. 18275–18284, Aug. 2019, doi: 10.1039/C9TA06084G.
[107] N. K. Noel *et al.*, "A low viscosity, low boiling point, clean solvent system for the rapid crystallisation of highly specular perovskite films," *Energy Environ. Sci.*, vol. 10, no. 1, pp. 145–152, 2017, doi: 10.1039/c6ee02373h.
[108] C. Wu *et al.*, "Cost-effective sustainable-engineering of CH3NH3PbI3 perovskite solar cells through slicing and restacking of 2D layers," *Nano Energy*, vol. 36, pp. 295–302, 2017, doi: 10.1016/j.nanoen.2017.04.034.
[109] H. Chen *et al.*, "A solvent-and vacuum-free route to large-area perovskite films for efficient solar modules," *Nature*, vol. 550, no. 7674, pp. 92–95, 2017, doi:

10.1038/nature23877.
[110] Y. Zhou *et al.*, " Thin-Film Transformation of NH 4 PbI 3 to CH 3 NH 3 PbI 3 Perovskite: A Methylamine-Induced Conversion-Healing Process ," *Angew. Chemie Int. Ed.*, vol. 55, no. 47, pp. 14723–14727, 2016, doi: 10.1002/anie.201609529.
[111] N. J. Jeon *et al.*, "Compositional engineering of perovskite materials for high-performance solar cells," *Nature*, vol. 517, no. 7535, pp. 476–480, 2015, doi: 10.1038/nature14133.
[112] W. S. Yang *et al.*, "Iodide management in formamidinium-lead-halide-based perovskite layers for efficient solar cells.," *Science.*, vol. 356, no. 6345, pp. 1376–1379, Jun. 2017, doi: 10.1126/science.aan2301.
[113] W. S. Yang *et al.*, "High-performance photovoltaic perovskite layers fabricated through intramolecular exchange," *Science.*, vol. 348, no. 6240, pp. 1234–1237, 2015, doi: 10.1126/science.aaa9272.
[114] M. Saliba *et al.*, "Incorporation of rubidium cations into perovskite solar cells improves photovoltaic performance," *Science.*, vol. 354, no. 6309, pp. 206–209, 2016, doi: 10.1126/science.aah5557.
[115] T. Zhao *et al.*, "Design rules for the broad application of fast (<1 s) methylamine vapor based, hybrid perovskite post deposition treatments," *RSC Adv.*, vol. 6, no. 33, pp. 27475–27484, 2016, doi: 10.1039/c6ra03485c.
[116] Y. Zhang *et al.*, "Trash into Treasure: δ-FAPbI3 Polymorph Stabilized MAPbI3 Perovskite with Power Conversion Efficiency beyond 21%," *Adv. Mater.*, vol. 30, no. 22, p. 1707143, 2018, doi: 10.1002/adma.201707143.
[117] Y. Zhang, S.-G. Kim, D.-K. Lee, and N.-G. Park, "$CH_3NH_3PbI_3$ and $HC(NH_2)_2PbI_3$ Powders Synthesized from Low-Grade PbI_2 : Single Precursor for High-Efficiency Perovskite Solar Cells," *ChemSusChem*, vol. 11, no. 11, pp. 1813–1823, 2018, doi: 10.1002/cssc.201800610.
[118] D. Ramirez *et al.*, "Meso-Superstructured Perovskite Solar Cells: Revealing the Role of the Mesoporous Layer," *Under Rev.*, 2018, doi: 10.1021/acs.jpcc.8b07124.
[119] P. Gratia *et al.*, "The Many Faces of Mixed Ion Perovskites: Unraveling and Understanding the Crystallization Process," *ACS Energy Lett.*, vol. 2, no. 12, pp. 2686–2693, Dec. 2017, doi: 10.1021/acsenergylett.7b00981.
[120] F. Ji *et al.*, "Simultaneous Evolution of Uniaxially Oriented Grains and Ultralow-Density Grain-Boundary Network in CH3NH3PbI3Perovskite Thin Films Mediated by Precursor Phase Metastability," *ACS Energy Lett.*, vol. 2, no. 12, pp. 2727–2733, 2017, doi: 10.1021/acsenergylett.7b00980.
[121] N. K. Noel *et al.*, "Highly Crystalline Methylammonium Lead Tribromide Perovskite Films for Efficient Photovoltaic Devices," *ACS Energy Lett.*, vol. 3, no. 6, pp. 1233–1240, 2018, doi: 10.1021/acsenergylett.8b00509.
[122] A. A. Petrov *et al.*, "Crystal Structure of DMF-Intermediate Phases Uncovers the Link Between CH 3 H 3PbI 3 Morphology and Precursor Stoichiometry," *J. Phys. Chem. C*, vol. 121, no. 38, pp. 20739–20743, 2017, doi: 10.1021/acs.jpcc.7b08468.
[123] G. C. Papavassiliou, "Synthetic Three-and Lower- Dimensional Semiconductors Based on Inorganic Units," *Mol. Cryst. Liq. Cryst. Sci. Technol. . Sect. A . Mol. Cryst. Liq. Cryst.*, vol. 286, no. 1, pp. 231–238, 2006, doi: 10.1080/10587259608042291.
[124] J. Cao *et al.*, "Identifying the Molecular Structures of Intermediates for Optimizing the Fabrication of High-Quality Perovskite Films," *J. Am. Chem. Soc.*, vol. 138, no. 31,

pp. 9919–9926, 2016, doi: 10.1021/jacs.6b04924.
[125] Y. Fu *et al.*, “Stabilization of the Metastable Lead Iodide Perovskite Phase via Surface Functionalization,” *Nano Lett.*, vol. 17, no. 7, pp. 4405–4414, 2017, doi: 10.1021/acs.nanolett.7b01500.
[126] J. C. Hamill, J. Schwartz, and Y. Loo, “Influence of Solvent Coordination on Hybrid Organic − Inorganic Perovskite Formation,” *ACS Energy Lett.*, vol. 3, pp. 93–97, 2018, doi: 10.1021/acsenergylett.7b01057.
[127] M. Sandström, I. Persson, and P. Peerson, “A study of solvent electron-pair donor ability and lewis basicity scales,” *Acta Chem. Scand.*, vol. 44, pp. 653–675, 1990.
[128] J. Oszczapowicz, *Basicity, H-Bonding, tautomerism and complex formation of imidic acid derivatives. The Chemistry of Amidines and Imidates*. John Wiley & Sons Ltd., 1991.
[129] G. Häfelinger, “General and theoretical aspects of amidines and imidic acid derivatives,” in *The Chemistry of Amidines and Imidates*, 2010, pp. 1–677.
[130] J. C. Grivas and A. Taurins, “Reaction of Trichloroacetonitrile With Primary and Secondary Amines,” *Can. J. Chem.*, vol. 36, no. 1958, pp. 771–774, 1958.
[131] L. Q. Xie *et al.*, “Understanding the Cubic Phase Stabilization and Crystallization Kinetics in Mixed Cations and Halides Perovskite Single Crystals,” *J. Am. Chem. Soc.*, vol. 139, no. 9, pp. 3320–3323, 2017, doi: 10.1021/jacs.6b12432.
[132] S. Rahimnejad, A. Kovalenko, S. M. Forés, C. Aranda, and A. Guerrero, “Coordination Chemistry Dictates the Structural Defects in Lead Halide Perovskites,” *ChemPhysChem*, vol. 17, no. 18, pp. 2795–2798, 2016, doi: 10.1002/cphc.201600575.
[133] J. W. Lee, H. S. Kim, and N. G. Park, “Lewis Acid-Base Adduct Approach for High Efficiency Perovskite Solar Cells,” *Acc. Chem. Res.*, vol. 49, no. 2, pp. 311–319, 2016, doi: 10.1021/acs.accounts.5b00440.
[134] H. Zhang, Y. Lv, J. Wang, H. Ma, Z. Sun, and W. Huang, “Energy , Environmental , and Catalysis Applications Influence of Cl incorporation in perovskite precursor on crystal growth and storage-stability of perovskite solar cells Influence of Cl incorporation in perovskite precursor on crystal growth and storage,” 2019, doi: 10.1021/acsami.8b19390.
[135] D. P. McMeekin *et al.*, “A mixed-cation lead mixed-halide perovskite absorber for tandem solar cells,” *Science.*, vol. 351, no. 6269, pp. 151–155, 2016, doi: 10.1126/science.aad5845.
[136] E. Edri, S. Kirmayer, D. Cahen, and G. Hodes, “High Open-Circuit Voltage Solar Cells Based on Organic–Inorganic Lead Bromide Perovskite,” *J. Phys. Chem. Lett.*, vol. 4, no. 6, pp. 897–902, Mar. 2013, doi: 10.1021/jz400348q.
[137] M. I. Saidaminov *et al.*, “High-quality bulk hybrid perovskite single crystals within minutes by inverse temperature crystallization,” *Nat. Commun.*, vol. 6, no. May, pp. 1–6, 2015, doi: 10.1038/ncomms8586.
[138] W. Ke, I. Spanopoulos, C. C. Stoumpos, and M. G. Kanatzidis, “Myths and reality of HPbI3 in halide perovskite solar cells,” *Nat. Commun.*, vol. 9, no. 1, p. 4785, 2018, doi: 10.1038/s41467-018-07204-y.
[139] P. M. Bodhankar, P. B. Sarawade, G. Singh, A. Vinu, and D. S. Dhawale, “Recent advances in highly active nanostructured NiFe LDH catalyst for electrochemical water splitting,” *J. Mater. Chem. A*, vol. 9, no. 6, pp. 3180–3208, 2021, doi: 10.1039/d0ta10712c.

[140] F. Dionigi and P. Strasser, “NiFe-Based (Oxy)hydroxide Catalysts for Oxygen Evolution Reaction in Non-Acidic Electrolytes,” *Adv. Energy Mater.*, vol. 6, no. 23, 2016, doi: 10.1002/aenm.201600621.
[141] L. Wu *et al.*, “Recent Advances in Self-Supported Layered Double Hydroxides for Oxygen Evolution Reaction,” *Research*, vol. 2020, pp. 1–17, 2020, doi: 10.34133/2020/3976278.
[142] Y. Xu *et al.*, “Room-temperature synthetic NiFe layered double hydroxide with different anions intercalation as an excellent oxygen evolution catalyst,” *RSC Adv.*, vol. 5, pp. 55131–55135, 2015, doi: 10.1039/b000000x.
[143] H. Li, X. Wang, T. Wang, and F. Xiao, “A facile, green and time-saving method to prepare partially crystalline NiFe layered double hydroxide nanosheets on nickel foam for superior OER catalysis,” *J. Alloys Compd.*, vol. 844, p. 156224, 2020, doi: 10.1016/j.jallcom.2020.156224.
[144] B. M. Hunter, W. Hieringer, J. R. Winkler, H. B. Gray, and A. M. Müller, “Effect of interlayer anions on [NiFe]-LDH nanosheet water oxidation activity,” *Energy Environ. Sci.*, vol. 9, no. 5, pp. 1734–1743, 2016, doi: 10.1039/c6ee00377j.
[145] A. A. Kashale, C. H. Yi, K. Y. Cheng, J. S. Guo, Y. H. Pan, and I. W. P. Chen, “Binder-free heterostructured NiFe2O4/NiFe LDH nanosheet composite electrocatalysts for oxygen evolution reactions,” *ACS Appl. Energy Mater.*, vol. 3, no. 11, pp. 10831–10840, 2020, doi: 10.1021/acsaem.0c01863.
[146] J. Jin *et al.*, “Exceptional electrocatalytic oxygen evolution efficiency and stability from electrodeposited NiFe alloy on Ni foam,” *Electrochim. Acta*, vol. 299, pp. 567–574, 2019, doi: 10.1016/j.electacta.2019.01.026.
[147] R. Chen *et al.*, “Achieving stable and efficient water oxidation by incorporating NiFe layered double hydroxide nanoparticles into aligned carbon nanotubes,” *Nanoscale Horizons*, vol. 1, no. 2, pp. 156–160, 2016, doi: 10.1039/c5nh00082c.
[148] R. Chen *et al.*, “Layered Structure Causes Bulk NiFe Layered Double Hydroxide Unstable in Alkaline Oxygen Evolution Reaction,” *Adv. Mater.*, vol. 31, no. 41, pp. 1–7, 2019, doi: 10.1002/adma.201903909.
[149] P. Wang and B. Wang, “Interface Engineering of Binder-Free Earth-Abundant Electrocatalysts for Efficient Advanced Energy Conversion,” *ChemSusChem*, vol. 13, no. 18, pp. 4795–4811, 2020, doi: 10.1002/cssc.202001293.
[150] D. R. G. Mitchell, “DiffTools: Electron diffraction software tools for DigitalMicrograph™,” *Microsc. Res. Tech.*, vol. 71, no. 8, pp. 588–593, 2008, doi: 10.1002/jemt.20591.
[151] F. Song and X. Hu, “Exfoliation of layered double hydroxides for enhanced oxygen evolution catalysis,” *Nat. Commun.*, vol. 5, p. 4477, 2014, doi: 10.1038/ncomms5477.
[152] S. Sirisomboonchai *et al.*, “Fabrication of NiO Microflake@NiFe-LDH Nanosheet Heterostructure Electrocatalysts for Oxygen Evolution Reaction,” *ACS Sustain. Chem. Eng.*, vol. 7, no. 2, pp. 2327–2334, 2019, doi: 10.1021/acssuschemeng.8b05088.
[153] X. Xue *et al.*, “One-step synthesis of nickel-iron layered double hydroxides with tungstate acid anions: Via flash nano-precipitation for the oxygen evolution reaction,” *Sustain. Energy Fuels*, vol. 3, no. 1, pp. 237–244, 2019, doi: 10.1039/c8se00394g.
[154] J. W. Zhao, Z. X. Shi, C. F. Li, L. F. Gu, and G. R. Li, “Boosting the electrocatalytic performance of NiFe layered double hydroxides for the oxygen evolution reaction by exposing the highly active edge plane (012),” *Chem. Sci.*, vol. 12, no. 2, pp. 650–659,

2021, doi: 10.1039/d0sc04196c.
[155] Q. Q. Chen, C. C. Hou, C. J. Wang, X. Yang, R. Shi, and Y. Chen, “Ir4+-Doped NiFe LDH to expedite hydrogen evolution kinetics as a Pt-like electrocatalyst for water splitting,” *Chem. Commun.*, vol. 54, no. 49, pp. 6400–6403, 2018, doi: 10.1039/c8cc02872a.
[156] T. S. Munonde, H. Zheng, and P. N. Nomngongo, “Ultrasonic exfoliation of NiFe LDH/CB nanosheets for enhanced oxygen evolution catalysis,” *Ultrason. Sonochem.*, vol. 59, no. June, p. 104716, 2019, doi: 10.1016/j.ultsonch.2019.104716.
[157] M. Rosa, V. C. Bassetto, H. H. Girault, A. Lesch, and V. Esposito, “Assembling Ni-Fe Layered Double Hydroxide 2D Thin Films for Oxygen Evolution Electrodes,” *ACS Appl. Energy Mater.*, vol. 3, no. 1, pp. 1017–1026, 2020, doi: 10.1021/acsaem.9b02055.
[158] R. Thomas, T. Mathavan, M. A. Jothirajan, H. H. Somaily, H. Y. Zahran, and I. S. Yahia, “An effect of lanthanum doping on physical characteristics of FTO thin films coated by nebulizer spray pyrolysis technique,” *Opt. Mater. (Amst).*, vol. 99, no. September, p. 109518, 2020, doi: 10.1016/j.optmat.2019.109518.
[159] O. Diaz-Morales, I. Ledezma-Yanez, M. T. M. Koper, and F. Calle-Vallejo, “Guidelines for the Rational Design of Ni-Based Double Hydroxide Electrocatalysts for the Oxygen Evolution Reaction,” *ACS Catal.*, vol. 5, no. 9, pp. 5380–5387, 2015, doi: 10.1021/acscatal.5b01638.
[160] R. Chen *et al.*, “Use of Platinum as the Counter Electrode to Study the Activity of Nonprecious Metal Catalysts for the Hydrogen Evolution Reaction,” *ACS Energy Lett.*, vol. 2, no. 5, pp. 1070–1075, 2017, doi: 10.1021/acsenergylett.7b00219.
[161] Y. Tang, Q. Liu, L. Dong, H. Bin Wu, and X. Y. Yu, “Activating the hydrogen evolution and overall water splitting performance of NiFe LDH by cation doping and plasma reduction,” *Appl. Catal. B Environ.*, vol. 266, no. September 2019, p. 118627, 2020, doi: 10.1016/j.apcatb.2020.118627.
[162] Z. Qiu, C. W. Tai, G. A. Niklasson, and T. Edvinsson, “Direct observation of active catalyst surface phases and the effect of dynamic self-optimization in NiFe-layered double hydroxides for alkaline water splitting,” *Energy Environ. Sci.*, vol. 12, no. 2, pp. 572–581, 2019, doi: 10.1039/c8ee03282c.
[163] H. S. Jadhav, A. Roy, B. Z. Desalegan, and J. G. Seo, “An advanced and highly efficient Ce assisted NiFe-LDH electrocatalyst for overall water splitting,” *Sustain. Energy Fuels*, vol. 4, no. 1, pp. 312–323, 2019, doi: 10.1039/c9se00700h.
[164] H. Zhou *et al.*, “Layered NiFe-LDH/MXene nanocomposite electrode for high-performance supercapacitor,” *Int. J. Hydrogen Energy*, vol. 45, no. 23, pp. 13080–13089, 2020, doi: 10.1016/j.ijhydene.2020.03.001.
[165] Q. Fu *et al.*, “Recent Progress on the Long-Term Stability of Perovskite Solar Cells,” *Adv. Sci.*, vol. 5, no. 5, 2018, doi: 10.1002/advs.201700387.
[166] L. T. Schelhas *et al.*, “Insights into operational stability and processing of halide perovskite active layers,” *Energy Environ. Sci.*, 2019, doi: 10.1039/c8ee03051k.
[167] J. A. Christians, S. N. Habisreutinger, J. J. Berry, and J. M. Luther, “Stability in Perovskite Photovoltaics: A Paradigm for Newfangled Technologies,” *ACS Energy Lett.*, pp. 2136–2143, 2018, doi: 10.1021/acsenergylett.8b00914.
[168] I. S. Kim, M. J. Pellin, and A. B. F. Martinson, “Acid-Compatible Halide Perovskite Photocathodes Utilizing Atomic Layer Deposited TiO2 for Solar-Driven Hydrogen

Evolution," *ACS Energy Lett.*, vol. 4, no. 1, pp. 293–298, 2019.
[169] J. Liang *et al.*, "A Low-Cost and High-Efficiency Integrated Device toward Solar-Driven Water Splitting," *ACS Nano*, vol. 14, no. 5, pp. 5426–5434, 2020, doi: 10.1021/acsnano.9b09053.
[170] M. Jošt *et al.*, "Textured interfaces in monolithic perovskite/silicon tandem solar cells: Advanced light management for improved efficiency and energy yield," *Energy Environ. Sci.*, vol. 11, no. 12, pp. 3511–3523, 2018, doi: 10.1039/c8ee02469c.
[171] J. Jia *et al.*, "Solar water splitting by photovoltaic-electrolysis with a solar-to-hydrogen efficiency over 30%," *Nat. Commun.*, vol. 7, no. May, pp. 1–6, 2016, doi: 10.1038/ncomms13237.
[172] G. F. Samu and C. Janáky, "Photocorrosion at Irradiated Perovskite/Electrolyte Interfaces," *J. Am. Chem. Soc.*, vol. 142, no. 52, pp. 21595–21614, 2020, doi: 10.1021/jacs.0c10348.
[173] A. Al-Ashouri *et al.*, "Monolithic perovskite/silicon tandem solar cell with >29% efficiency by enhanced hole extraction," *Science.*, vol. 370, no. 6522, pp. 1300–1309, 2020, doi: 10.1126/science.abd4016.
[174] J. Azevedo *et al.*, "Tin oxide as stable protective layer for composite cuprous oxide water-splitting photocathodes," *Nano Energy*, vol. 24, pp. 10–16, 2016, doi: 10.1016/j.nanoen.2016.03.022.
[175] A. Al-Ashouri *et al.*, "Conformal monolayer contacts with lossless interfaces for perovskite single junction and monolithic tandem solar cells," *Energy Environ. Sci.*, vol. 12, no. 11, pp. 3356–3369, 2019, doi: 10.1039/c9ee02268f.
[176] M. Jošt, L. Kegelmann, L. Korte, and S. Albrecht, "Monolithic Perovskite Tandem Solar Cells: A Review of the Present Status and Advanced Characterization Methods Toward 30% Efficiency," *Adv. Energy Mater.*, doi: 10.1002/aenm.201904102.
[177] H. B. Profijt, S. E. Potts, M. C. M. van de Sanden, and W. M. M. Kessels, "Plasma-Assisted Atomic Layer Deposition: Basics, Opportunities, and Challenges," *J. Vac. Sci. Technol. A Vacuum, Surfaces, Film.*, vol. 29, no. 5, p. 050801, 2011, doi: 10.1116/1.3609974.
[178] A. E. A. Bracesco *et al.*, "The chemistry and energetics of the interface between metal halide perovskite and atomic layer deposited metal oxides," *J. Vac. Sci. Technol. A*, vol. 38, no. 6, p. 063206, 2020, doi: 10.1116/6.0000447.
[179] M. Gebhard *et al.*, "An efficient PE-ALD process for TiO2 thin films employing a new Ti-precursor," *J. Mater. Chem. C*, vol. 4, no. 5, pp. 1057–1065, 2016, doi: 10.1039/c5tc03385c.
[180] N. G. Kubala, P. C. Rowlette, and C. A. Wolden, "Plasma-enhanced atomic layer deposition of anatase TiO2 Using TiCl4," *J. Phys. Chem. C*, vol. 113, no. 37, pp. 16307–16310, 2009, doi: 10.1021/jp907266c.
[181] Y. Wang *et al.*, "Performance enhancement of perovskite solar cells via modification of the TiO2/perovskite interface with oxygen plasma treatment," *Thin Solid Films*, vol. 696, no. May 2019, p. 137786, 2020, doi: 10.1016/j.tsf.2020.137786.
[182] C. Ding, J. Shi, Z. Wang, and C. Li, "Photoelectrocatalytic Water Splitting: Significance of Cocatalysts, Electrolyte, and Interfaces," *ACS Catal.*, vol. 7, no. 1, pp. 675–688, 2017, doi: 10.1021/acscatal.6b03107.
[183] H. H. Lee *et al.*, "Optimal n-type al-doped zno overlayers for charge transport enhancement in p-type cu2 o photocathodes," *Micromachines*, vol. 12, no. 3, 2021,

doi: 10.3390/mi12030338.